CFD Modeling of a Novel 50 kW_{th} Indirectly Heated Bubbling Fluidized Bed Steam Reformer.

A.R. Ajodhia

Technische Universiteit Delft

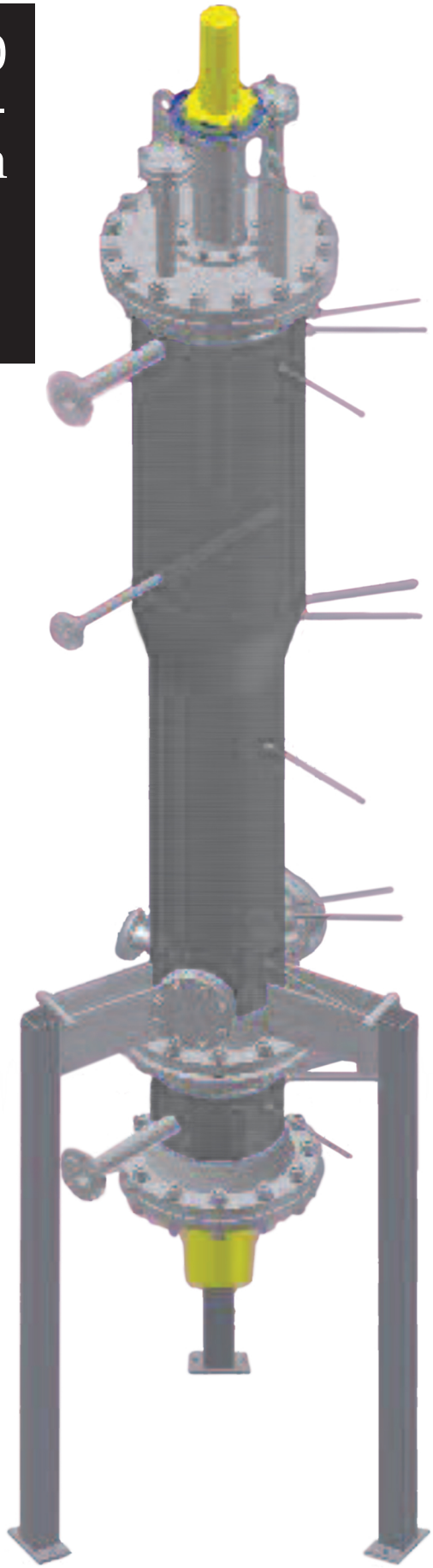

TU Delft Delft University of Technology

Challenge the future

CFD Modeling of a Novel 50 kW$_{th}$ Indirectly Heated Bubbling Fluidized Bed Steam Reformer.

by

A.R. Ajodhia

in partial fulfillment of the requirements for the degree of

Master of Science
in Mechanical Engineering

at the Delft University of Technology,

Student number:	4091833	
Supervisor:	Prof. dr. ir. W. de Jong	TU Delft
Thesis committee:	Prof. dr. ir. D. Roekaerts	TU Delft
	Prof. dr. ir. J. Padding	TU Delft
	Ir. M. del Grosso	TU Delft
	Dr. ir. E. Moghaddam	TU Delft

TU Delft Delft University of Technology

ACKNOWLEDGEMENT

The journey of writing this thesis had its ups and downs and some speed bumps along the way, but I managed to persevere thanks to the support of my supervisors, family and friends. First I'd like to thank my supervisor Prof. dr. ir. Wiebren de Jong and daily supervisor Ir. Mara del Grosso for being patient and understanding in regards to my personal situation. Second I'd like to thank dr. ir. Elyas Moghaddam for the supervision of the CFD modeling in ANSYS® Fluent, and offering his personal computer to use as a workplace. Countless simulations have been run with results ranging from non-explainable to somewhat satisfactory. I look back with fond memories brainstorming with both Mara and Elyas, trying to make sense of the numerical results and figuring out ways to improve on them. Lastly, I would like to thank my friends and family, being there for me through both the bad and the good days. I could count on them for advice and being there for me when something went wrong. This report would not have been possible without the support from everyone and I'm eternally grateful.

Akash Ajodhia

Delft, June 2nd, 2019

ABSTRACT

The Process and Energy department of the 3mE faculty of TU Delft and the Dutch company Petrogas Gas-Systems B.V. are working together on the commissioning of a small 50 kW_{th} Indirectly Heated Bubbling Fluidized Bed Steam Reformer (IHBFB-SR) heated by two radiant tube burners placed vertically inside the reactor. This is a new approach on indirectly heating as the heat is released from the inside to the outside, compared to existing indirectly heated gasifiers, where the heat is released from the outside to the inside.

The main objective of this thesis has been to analyze the hydrodynamics and heat transfer occurring within the reactor, by applying "Computational Fluid Dynamics" (CFD) techniques. The analysis has been carried out using the commercial CFD software ANSYS® FLUENT. First the physical phenomena occurring within the reactor have been identified and then research was done on the models and parameters developed to describe the physical phenomena. First the hydrodynamic behaviour was evaluated and then it was looked into how the heat transfer can be coupled to the hydrodynamics in the reactor.

In regards to the hydrodynamics, the Euler-Euler Two-Fluid Model (TFM) has been found to be appropriate, and the inter-phase drag coefficient was chosen as a parameter of interest. The Gidaspow drag model and the Syamlal-O-Brien model were compared to one another, and the solid volume fraction, pressure, axial velocity and granular temperature within the reactor were evaluated. The results were compared to the numerical solutions obtained in previous work, in order to understand which model gives a better prediction. The Gidaspow drag model was found to provide a better prediction of the core annular flow in the bed zone, and was therefore implemented in the heat transfer evaluation.

In regards to the heat transfer, models were already developed for the conductive and convective heat transfer in multiphase flows. For radiation there is still a lack of rigorous coupling between radiative heat transfer and hydrodynamics in simulations of non-dilute multiphase flows. The heat transfer simulation was performed in two steps, first with only the conductive and convective heat transfer, and then with radiation added to the system. The thermal properties such as the thermal conductivity, absorption and scattering coefficient have been made dependent of the volume fraction. For the case without radiation, a small temperature increase was observed with high temperature gradients near the wall. For the case with radiation, the Discrete-Ordinates (DO) Radiation model was evaluated. From the results it can be concluded that the DO Radiation model overpredicts the radiation that is emitted and scattered from the bed, causing the bed to heat up continuously to temperatures much higher than the radiant tube. More research and experimental validation is required in order to improve the coupling of the radiative heat transfer to the hydrodynamics.

CONTENTS

LIST OF FIGURES

LIST OF TABLES

NOMENCLATURE

Math symbols		*Unit*
A	Surface	m^2
a	Absorption Coefficient	m^{-1}-
A_r	Archimedes Number	-
b	Wien's displacement constant	m K
C	Linear anisotropic constant	-
C_p	Specific Heat	$J\,K^{-1}$
c_o	Speed of light	$m\,s^{-1}$
d	Diameter	m
$E_{b\lambda}$	Black Body Radiation Intensity	$W\,sr^{-1}\,m^{-2}$
e	Emmisivity	-
e_{ss}	Restitution Coefficient	-
g	Gravity Constant	$m\,s^{-2}$
H	Height	m
h	Heat Transfer Coefficient	$W\,m^{-2}\,K^{-1}$
h_P	Planck's constant	J s
J	Heat Flux	$W\,m^{-2}$
k	Thermal Conductivity	$W\,m^{-1}\,K^{-1}$
k_B	Boltzmann Constant	$J\,K^{-1}$
L	Length	m
M	Mass	kg
$\dot{m}$	Mass flow	$kg\,s^{-1}$
n	Index of refraction	-
Nu	Nusselt Number	-
Pr	Prandtl Number	-
P, p	Pressure	Pa
Q_{abs}	Absorption Efficiency	-
Q_{scat}	Scattering Efficiency	-
Q_{ext}	Extinction Efficiency	-
Q, q	Heat Flux	$W\,m^{-2}$
R	Universal Gas Constant	$J\,mol^{-1}K^{-1}$
Re	Reynolds Number	-
r	Radius	m
T	Temperature	K
t	Time	s
U, v	Velocity	$m\,s^{-1}$
x	Size parameter	-

Greek symbols		*Unit*
α	Volume Fraction	-
β	Interphase Drag Coefficient	kg m^{-3} s^{-1}
β_s	Extinction Coefficient	m^{-1}
λ	Wavelength	m
ϵ	Voidage	-
η	Efficiency	-
γ_s	Dissipation Energy	W m^{-3}
κ	Diffusion Coefficient for granular conductivity	kg m^{-1} s^{-1}
ρ	Density	kg m^{-3}
ρ^s	Hemispherical Emmisivity	-
ϕ	Sphericity	-
σ	Stephan Boltzmann Constant	W m^{-2}K^{-4}
σ_s	Scattering Coefficient	m^{-1}
Θ	Granular Temperature	m^{-2}s^{-2}
τ	Optical Thickness	m
μ	Viscosity	Pa s

Subscripts

b	Bed
g	Gas
mf	Minimum Fluidization
max	Maximum
p	Particle
r	Reactor
s	Solid

Abbreviations

BFB	Bubbling Fluidized Bed
CFB	Circulating Fluidized Bed
CFD	Computational Fluid Dynamics
DDPM	Dense Discrete Phase model
CV	Control Volume
DO	Discrete Ordinates
DTRM	Discrete Transfer Radiation Model
FICFB	Fast Internally Circulating Fluidized Bed
IGCC	Integrated Gasification Combined Cycle
IH-BFBSR	Indirectly Heated Bubbling Fluidized Bed Steam Reformer
KTGF	Kinetic Theory of Granular Flow
RTE	Radiative transfer equation
S2S	Surface to Surface
TFM	Two Fluid Model

1

INTRODUCTION

1.1. PROJECT INTRODUCTION

In cooperation with Petrogas Gas-Systems, TU Delft has been involved in the design, engineering, commissioning and operation of a 50 kWth Indirectly Heated Bubbling Fluidized Bed Steam Reformer [IH-BFBSR] heated by two radiant tube burners placed vertically inside the reactor. An analysis on its capabilities is performed and new models can be developed and validated related to overall performance characteristics like gas composition of main and minor species and details of heat transfer characteristics.
Schouten [14] researched the viability of the proposed technology and possible basic reactor designs by modelling in Aspen Plus ® and conducting hydrodynamic experiments. This project is a continuation of the research done by Schouten [14] and focuses on the microscopic modelling of the hydrodynamics and heat transfer processes that play a role within the IH-BFBSR. A good simulation model of a gasifier or steam reformer can provide valuable information and is essential in designing a good experimental or commercial setup.

1.2. BIOMASS INCENTIVE

The world energy consumption has increased exponentially during the last century estimated to be around 13864.9 Mtoe in 2019, where approximately 84% of this energy still finds its origin in fossil fuels as can be seen in Figure 1.1 [1]. With the growing awareness of the depletion of fossil fuel sources and the dangers of increasing CO_2 levels in the atmosphere due to fossil fuel usage, several measures are being taken to pursue energy sustainability, which can be summarized by the "Trias Energetica" model which was developed in 1979 at the Technical University Delft by Kees Duijvestein [16].

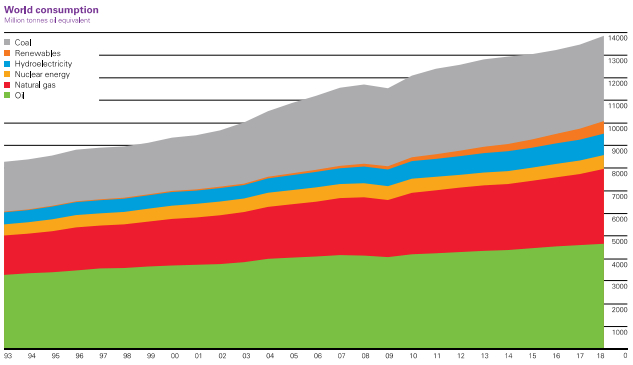

Figure 1.1: World primary energy consumption in Mtoe per year 2019 [1]

The "Trias Energetica" makes clear that energy savings have to come first on the path to environmental protection. First, the energy demand must be decreased through energy saving. Second, renewable sources should be used to meet the remaining energy demand (e.g. biomass, sun & wind). Third, (conventional) energy conversion systems must be designed and developed to increase the energy efficiency and reduce the production of environmentally harmful residuals and exhaust gasses (e.g.

"Carbon Capture", "Integrated gasification combined cycles [IGCC]"). The "Trias Energetica" model is summarized in Figure 1.2 [2].

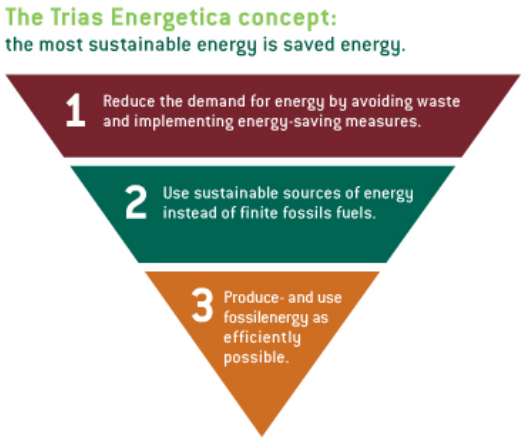

Figure 1.2: Trias Energetica steps [2]

.

1.3. BIOMASS GASIFICATION

Gasification is a relatively old technology with an upsurge in interest the past years fueled by several factors:

- Interest in the reduction in greenhouse gas emissions as a result of energy conversion.
- Push for independence from the less reliable supply and fluctuating prices of oil and gas.
- Interest in renewable and locally available energy sources [3].

Gasification is the thermochemical conversion of solid or liquid feedstock into useful gaseous fuel or chemical feedstock that can be burned to release energy or can be used for production of value-added chemicals as shown in Figure 1.3. The solid/liquid fuel reacts with a gasifying medium (oxidizing or reducing) usually at temperatures higher than 700°C. The gasifying medium can be air, pure oxygen, steam, carbon dioxide or a mixture of these gases. One of the drawbacks of biomass gasification is the co-production of tar and ash. Tar is produced by the partial oxidation of biomass described by a set of complex reaction equations. The tar can condense in downstream components and clog the entire system.

Ash production is common in biomass gasification due to their high alkali content. When the ashes are released, they can cause slagging, fouling or agglomeration to the bed material which results in defluidization problems in the reactor.

While gasification and combustion are closely related thermochemical processes, there is an important difference between them. Gasification packs energy into chemical bonds in the product gas; combustion breaks those bonds to release the energy. The gasification process is explained in more detail in Appendix D.

In order to increase the energy efficiency and reduce emissions of (coal based) energy systems, an integrated gasification combined cycle (IGCC) was developed, where the gasified fuel is first burnt in a combustion turbine-generator unit and then the hot exhaust gas from its gas turbine is used for generating steam to produce further power in a steam turbine–generator unit[7]. A schematic of a possible IGCC setup (including a heat recovery steam generator [HRSG]) is shown in Figure 1.4.

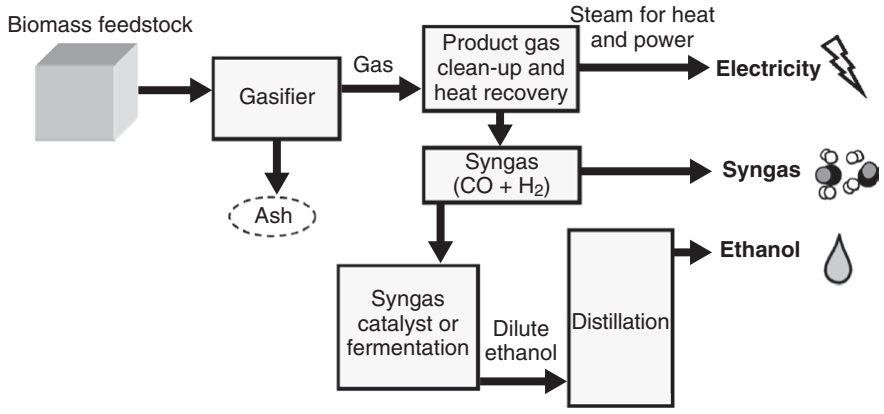

Figure 1.3: Thermochemical conversion route of biomass for the production of energy, gas, and ethanol [3].

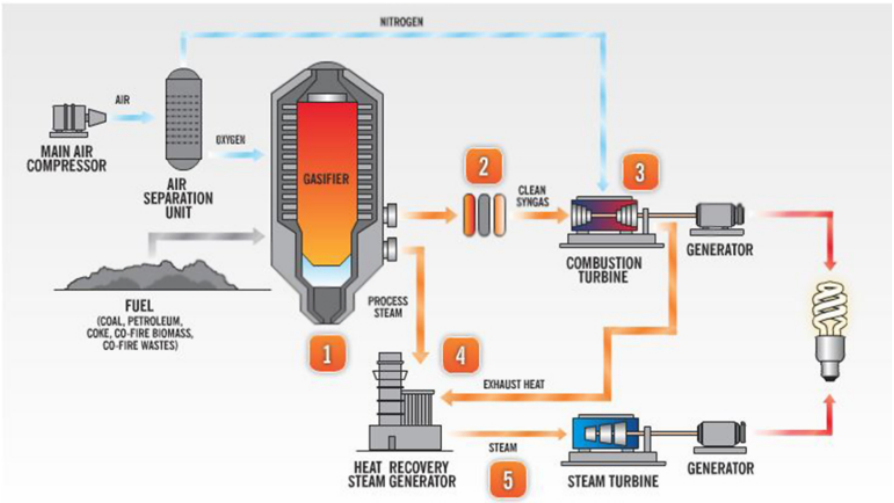

Figure 1.4: IGCC cycle [4].

Gasification is carried out generally in one of the three major types of gasifiers:

- Moving bed (also called a moving fixed bed).
- Fluidized bed.
- Entrained flow[3].

In the Netherlands there is a latent need for biomass conversion plants with sizes ranging from 5MW to 30 MW. Smaller plants have no commercial interest and bigger plants have difficulties in the supply of feedstock and distribution of produced heat [14]. Fluidized bed gasifiers are particularly suitable for medium-size units (<25 MW_{th}), thus gasifiers operating in the bubbling fluidized-bed regime are preferred [3].

1.4. FLUIDIZED BED GASIFIERS

The bubbling fluidized-bed gasifier was developed by Fritz Winkler in 1921 and is perhaps the oldest commercial application of fluidized beds used for many years for the gasification of coal. In a typical fluidized bed gasifier, solid fuel particles are fed into an oxygen- or air starved bed. The bed material consists of small heated inert solid particles such as sand. By feeding the gasifying medium at the bottom of the furnace, flowing upward, the particles in the bed are affected by drag forces depending on the velocity of the gasifying medium. At a certain inlet velocity, the minimum fluidization velocity U_{mf}, the frictional forces acting on the particles equal the gravitational forces, and the solid bed material starts behaving as a fluid. By further increasing the inlet velocity, a high degree of particle mixing is established, and the bed is fluidized.
Based on the degree of fluidization of the bed material, i.e. the inlet velocity of the steam, a distinction can be made between two different types of fluidized bed gasification; "Bubbling Fluidized Bed" (BFB)- and "Circulating Fluidized Bed" (CFB) gasification.

In a BFB the gas velocity is increased from the minimum fluidization velocity just enough to cause the emergence of a well-defined horizontal surface of the bed with bubbles and gas passages forming in the bed (usually around 2.5 times the minimum fluidization) [17]. The open space above the bed is called the freeboard. An illustration of a BFB is shown in Figure 1.5a.

The CFB is composed by a riser and a downcomer connected by a cyclone. In a CFB the fluidization velocity is so high that it can blow all solids out of the riser. The majority of the solids leaving the furnace is captured by the cyclone (a gas-solid separator) and is recirculated back to the base of the riser at a rate sufficiently high to cause a minimum degree of vertical mixing of solids in the furnace [7]. An illustration of a CFB is shown in Figure 1.5b.

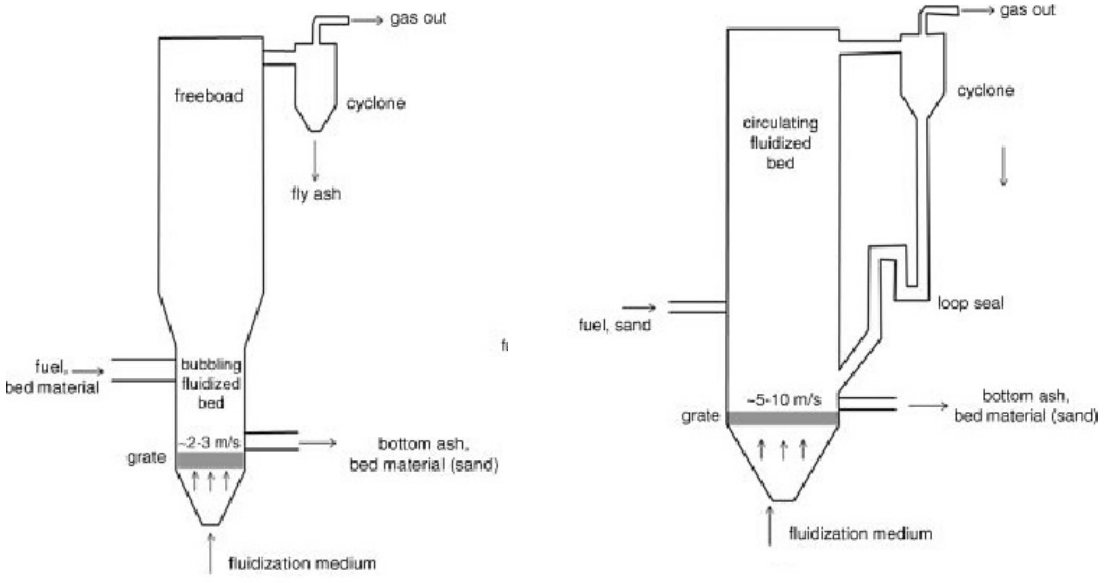

(a) BFB

(b) CFB

Figure 1.5: Schematics of fluidized beds [5].

The fluidized bed gasifier can also be distinguished based on the mode of heating:

- Directly heated: part of the fuel is oxidized to provide the heat needed for the endothermic gasification reactions.
- Indirectly heated: the heat needed for gasification is externally supplied by a hot inert medium which in turn is heated by the combustion of char or the produced flue gas in a separate reactor.[3]

Most gasifiers today are directly heated. The main advantage of an indirectly heated gasifier however is that the combustion products in partial oxidation are not mixed with the product gas. This results in a higher calorific value product gas which gives more utilization possibilities.

1.4.1. INDIRECTLY HEATED GASIFIERS

Examples of indirectly heated gasifiers include the "MILENA" developed by ECN in the Netherlands and the “heat pipe reformer” designed by the TU Munich in Germany.

The Milena gasifier is composed by separate coaxial sections for gasification and combustion as can be seen in Figure 1.6a. The gasification section consists of three parts: gasifier riser, settling chamber and downcomer while the combustion section consists of only one part where the unreacted char from the gasification is combusted to obtain the heat needed for the desired reactions [18].

In the Heatpipe reformer the reforming takes place in a pressurized vessel at 2 to 10 bar at 800 ^{o}C while a second chamber is used for the combustion of the char particles in order to provide heat for the gasification process. The heat transport occurs via so called heat pipes which are closed tubes that are filled with a small amount of liquid (sodium). By evaporation and condensation of this liquid, the heat is transferred to the top of the heatpipe. The cooled down liquid, then, flows back to the bottom by gravity and capillary effects into the evaporation zone [19] .

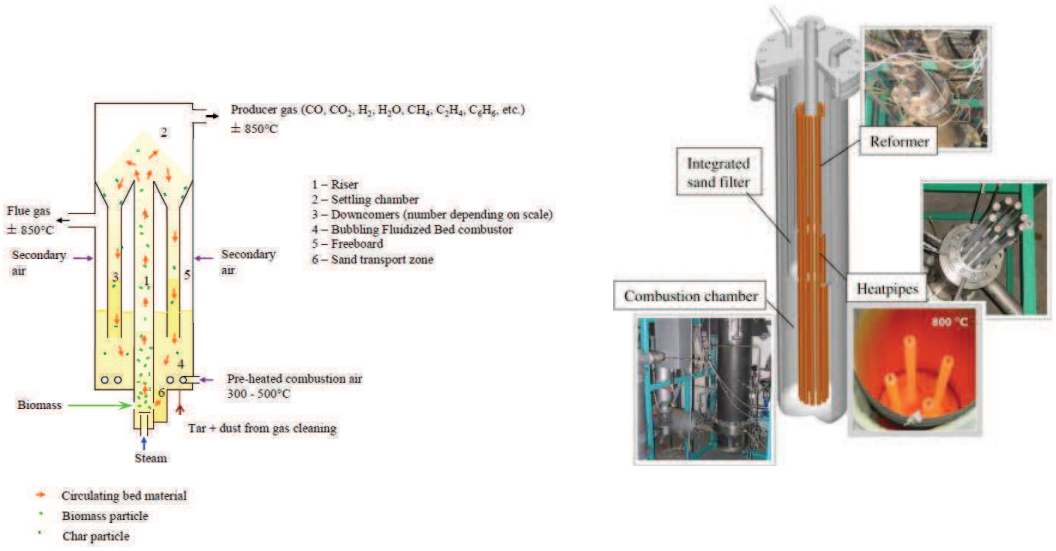

(a) Milena [18]. (b) Heatpipe reformer [20].

Figure 1.6: Simplified overview of indirectly heated gasifier designs.

The working principle of the MILENA and heat pipe reformer by TU Munich is shown in Figure 1.7.

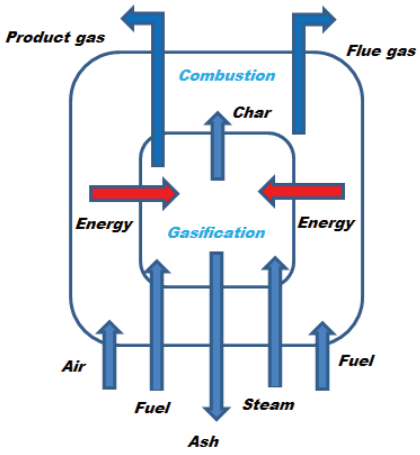

Figure 1.7: Working principle of Milena and Heatpipe reformer.

1.4.2. IH-BFBSR

Petrogas Gas-Systems and the TU Delft Process & Energy section are designing, engineering and commissioning a small 50 kW_{th} Indirectly Heated Bubbling Fluidized Bed Steam Reformer (IH-BFBSR) heated by two radiant tube burners placed vertically inside the reactor. The reforming takes place in an atmospheric bubbling fluidized bed gasifier at 850°C while the combustion occurs inside two burners placed vertically inside the reactor, one at the top and one at the bottom. The heat is transported indirectly by radiation via two radiant tubes. In this way gasification and combustion reactions take place separately leading to a higher quality of the gas obtained.

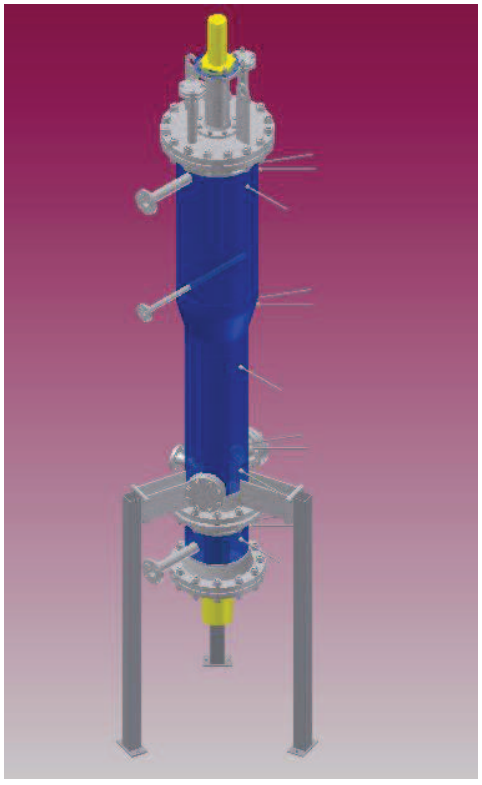

Figure 1.8: 3D drawing of the IH-BFBSR.

The working principle of the IH-BFBSR is shown in Figure 1.9.

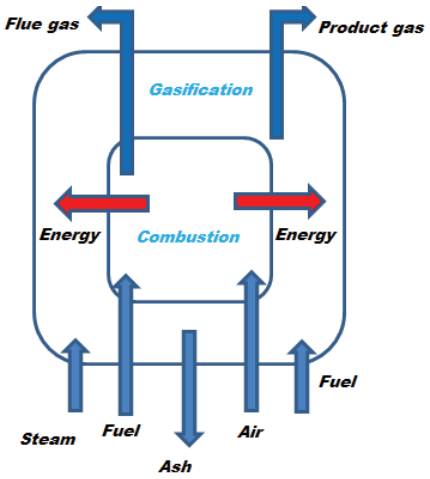

Figure 1.9: Working principle of the IH-BFBSR.

When comparing the working principle of the Milena and Heatpipe reformer to the IH-BFBSR, some main differences can be emphasized and they are summarized in Table 1.1:

Table 1.1: Main differences between IH-BFBSR and Milena/Heatpipe reformer.

IH-BFBSR	MILENA/HEATPIPE REFORMER
Heat released from inside to outside (burners and radiant tubes inside the fluidized bed reactor)	Heat released from outside to inside (combustion chamber around the reformer).
Unreacted char from gasification is not combusted	Combustion of the unreacted char from the gasification inside the combustor.

1.5. SCOPE OF THESIS

The IH-BFBSR represents a new concept of indirectly heating based on combustion. Multiphase flows occurring in the IH-BFBSR are quite complex and while experiments may provide better insight into the flow behaviour and heat transfer within the reactor, a numerical analysis like Computational Fluid Dynamics (CFD) is an attractive, cheaper, alternative solution, which can be compared to the results of well defined experiments.

The aim of this work is to apply a numerical approach to model the hydrodynamics and heat transfer of an indirectly heated bubbling fluidized bed. Problems involving the transport of momentum, mass and energy are chosen to be solved using commercial computational fluid dynamics (CFD) software ANSYS® FLUENT, because this enables a flexible and fast implementation. To do so, the following research questions have been formulated:

- Which hydrodynamic models have been developed that are applicable to multiphase flows occurring in the IH-BFBSR?
- Which heat transfer models (conduction, convection & radiation) have been developed applicable to multiphase flows occurring in the IH-BFBSR?
- Which parameters are required as input for the above mentioned models?
- How are the the models and parameters of interest (e.g. drag function, particles size, gasifying medium) implemented in CFD commercial software ANSYS® FLUENT.
- What hydrodynamic behaviour does the numerical solution predict, based on the chosen model and parameters (e.g. particle distribution & velocity, bed expansion)?

- What is the effect of the heat transfer models on the temperature distribution within the reactor?

1.6. OUTLINE OF THESIS

The thesis is arranged in 6 chapters:

- Chapter 2 presents a literature and technology overview of the IH-BFBSR, explaining the hydrodynamics and heat transfer mechanisms occurring in the reactor.
- Chapter 3 presents an overview of multiphase models that have been developed in recent years applicable to bubbling fluidized bed, and the parameters that are of interest.
- Chapter 4 explains the implementation process of the selected models and parameters in ANSYS® FLUENT.
- Chapter 5 presents the resulting hydrodynamic behaviour and temperature profiles based on different input parameters with the chosen models.
- Chapter 6 summarizes the results and provides suggestions for future work.

2

RESEARCH LITERATURE OVERVIEW

This chapter provides more insight into the design of the IH-BFBSR and the theory of the physical phenomena occurring within a BFB. The physical phenomena are divided into three parts: hydrodynamics, heat transfer and gasification.

2.1. REACTOR DESIGN SPECIFICATIONS

The design for the IH-BFBSR is depicted in Figure 2.1 and consists of three sections: the windbox, the bed zone and the freeboard.

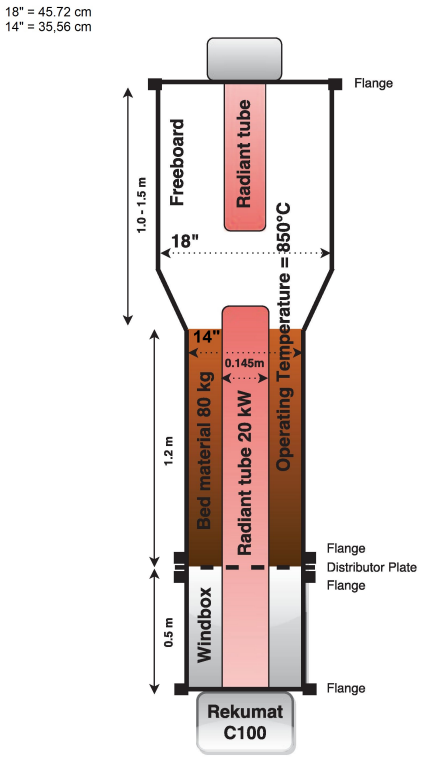

Figure 2.1: IH-BFBSR reactor design.

Two radiant tubes have been mounted to the bottom- and top side of the reactor in order to increase the heat transfer area thus improving the carbon and tar conversion. In order to limit the heat losses, the outside of the reactor is covered with insulation.

2.1.1. WINDBOX & DISTRIBUTOR PLATE

The windbox is the lowest section of the reactor and the steam supply is directly fed into this. Before the steam reaches the bed, it flows through a distributor plate.

The distributor plate is perforated, consisting of 50 tuyeres to prevent the back flow of solids. According to Zuiderweg and Drikenburg [21], the pressure drop Δp_d over the plate is sufficiently high to create a uniform gas distribution over the entire plate and is estimated to be (0.2 - 0.4) times the pressure drop over the bed Δp_b.

$$\Delta p_d = (0.2 - 0.4) \cdot \Delta p_b \tag{2.1}$$

The distributor plate used in the IH-BFBSR, is based on the design by Schwings Fluid Technologies [14].

2.1.2. BED ZONE

The bed can consist of sand, ash from the fuel or catalytically active materials such as dolomite or olivine. The bed material is used to distribute and transport the heat evenly in order to create a uniform temperature gradient along the reactor. This prevents local hot spots and maintains a proper mixing of the fuel.

Based on the fluidization behaviour, Geldart [12] classified the bed materials into four categories which are defined in Table 2.1.

Table 2.1: Geldart classification groups[12].

Group	
A	Particle size between 20 and 200 μm , density is typically less than 1.4 g/cm^3 . The beds made from these particles will expand with a factor of 2 to 3 when fluidized because the bulk density is relatively low.
B	Particle size between 40 and 500 μm, density is typically between 1.4 - 4 g/cm^3. Bubbling of the bed will mostly occur directly at fluidization and has bubbles that grow large.
C	Very fine powders and cohesive particles. Particle size between 20 and 30 μm. Hard to fluidize and may require an external force like mechanical agitation to properly fluidize. Flour and starch are typical powders for this group.
D	Larger particles, size above 600 μm and bulk density is also relatively large. Fluidization of these materials requires a large gas flow.

The bed material used in the IH-BFBSR setup is corundum Al_2O_3, has a density of 3950 kg/m^3 and a particle size around 352μm. Thus the particles belong in group B according to the Geldart classification. The particle size distribution can be viewed in Appendix C.

2.1.3. FREEBOARD

When increasing the gas inlet velocity above U_{mf}, bed particles are thrown up into the freeboard section. Some entrained particles are dragged upwards by the gas flow, while others are disengaged and fall back to the bed surface. The rate at which the particles are leaving the reactor is called the elutriation rate.

The height of the freeboard section is based on the "Transport Disengagement Height"(TDH). At the TDH the elutration rate becomes saturated and further increase of the height of the reactor will not affect the elutriation rate anymore.

The diameter in the freeboard section is expanded to reduce the gas velocity and therefore the elutriation of bed material, allowing particles to return to the bed zone. This results in a longer gas residence time that can improve the carbon and hydrocarbon conversion in the reactor.

2.1.4. RADIANT TUBE BURNERS

The heaters in the IH-BFBSR are combustion radiant tubes burners, chosen for their high heat flux and the ability to be used upside down which gives a very wide area of application. The radiant tubes in the IH-BFBSR design are the Rekumat C150, mounted at the bottom, and the Rekumat C100 mounted at the top of the reactor as seen in Figure 2.1.

2.2. HYDRODYNAMICS

Most of the environmental and operating characteristics within a fluidized bed gasifier are a direct result of the hydrodynamics of gas- solid interaction. The performance of the fluidized bed gasifier can drop significantly when the operation conditions are different from the designed fluidization regime. This chapter presents an overview of the hydrodynamics occurring in a fluidized bed gasifier.

2.2.1. FLUIDIZATION REGIMES

Fluidization is defined as the operation through which fine solids are transformed into a fluid-like state through contact with a gas or liquid and displays the following characteristics similar to those of a liquid:

- The static pressure at any height is approximately equal to the weight of the bed solids per unit of cross-sectional area above that level.
- An object denser than the bulk density of the bed will sink, while one lighter will float.
- The solids from the bed may be drained like a liquid through an orifice at the bottom or on the side of the container where the solids' flow-stream is similar to a water jet from a vessel.
- The bed surface maintains a horizontal level, independent of how the bed is tilted and assumes the shape of the vessel.
- Particles are well mixed, and the bed maintains a nearly uniform temperature throughout its body when heated.

With increasing gas velocity, a series of changes occur in the motion of the particles and this behavior can be categorized in the following regimes as seen in Figure 2.2 [7].

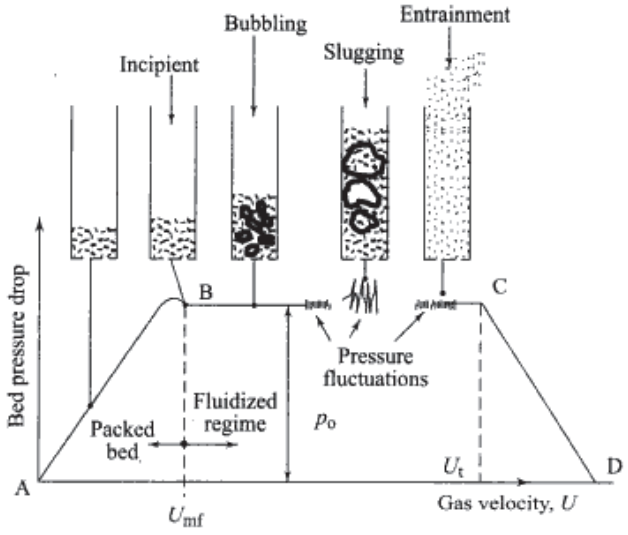

Figure 2.2: Variation of bed pressure drop with superficial velocity [6].

2.2.1.1. PACKED BED

At low fluidizing velocities, the gas will flow through the particles without moving them. The pressure drop over a packed bed $\triangle p_b$ increases linearly with the increasing gas velocity (A-B trajectory in Figure 2.2) till it is equal to the weight of the bed divided by its cross sectional area A_b, and can be rewritten as:

$$\triangle p_b A_b = M_b g, \tag{2.2}$$

where M_b is the mass of the bed and g the standard gravity ($9.81 m/s^2$). Assuming the bed particles are uniform in size, the pressure drop over the bed $\triangle p_b$ can be calculated by the Ergun's [22] equation:

$$\frac{\triangle p_b}{L_b} = 150\frac{(1-\epsilon)^2}{\epsilon^3}\frac{\mu_g U}{(\phi d_p)^2} + 1.75\frac{1-\epsilon}{\epsilon^3}\frac{\rho_g U^2}{\phi_p d_p}, \tag{2.3}$$

where U is the superficial velocity, L_b the length of the bed, ϵ the void fraction in the bed, d_p and ϕ_p the surface-volume mean diameter and sphericity of the particles, μ_g and ρ_g the viscosity and density of the gas respectively. The voidage ϵ is the fraction of the bed volume which is occupied by the space between the bed particles and is according to Basu [7], calculated as:

$$\epsilon = \frac{\text{volume of bed} - \text{volume of solids}}{\text{volume of bed}}. \tag{2.4}$$

The sphericity of a particle ϕ_p is according to Basu [7], defined as:

$$\phi_p = \frac{\text{surface area of a sphere of the same volume as the particle}}{\text{surface area of the particle}}. \tag{2.5}$$

The solids only move with respect to the wall, but not to one another.

2.2.1.2. FLUIDIZED REGIME

With a further increase in flow reaching the minimum fluidization velocity, the fixed bed transforms into an incipiently fluidized bed (point B in Figure 2.2). When a fluid flows over a stationary particle or travels at a velocity higher than a upward moving particle, the particle is subjected to an upward fluid drag, a buoyancy force and downward gravitational force as shown in Figure 2.3 [7].

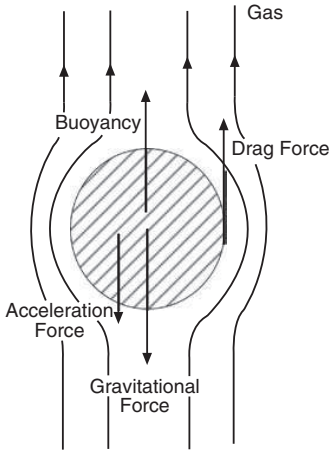

Figure 2.3: Force balance on a particle moving upwards [7].

The force balance under steady state conditions can be written as:

$$\text{Gravitational force} = \text{Buoyancy force} + \text{Drag force}. \tag{2.6}$$

As the pressure drop across the bed is equal to the weight of the bed (equation 2.2), the fluid drag F_D is calculated as:

$$F_D = \triangle p_b A_b = A_b L(1-\epsilon)(\rho_p - \rho_g)g. \tag{2.7}$$

At minimum fluidization conditions ($U = U_{mf}$), the voidage ϵ_{mf} is slightly higher than when at packed bed conditions. The minimum fluidization velocity U_{mf} can be calculated by solving equation 2.2 and 2.3 to obtain the dimensionless Reynolds number:

$$Re_{mf} = \frac{U_{mf} d_p \rho_g}{\mu} = [C_1^2 + C_2 Ar]^{0.5} - C_1, \tag{2.8}$$

where A_r is the dimensionless Archimedes number given by:

$$Ar = \frac{\rho_g(\rho_p - \rho_g) g d_p^3}{\mu^2}, \tag{2.9}$$

and C_1 & C_2 empirical Grace constants taken from experiments, being 27.2 and 0.0408 respectively [23].

When the gas flow goes beyond the minimum fluidization velocity ($U > U_{mf}$), the excess gas will flow in the form of bubbles. Bubbles are gas voids with very few or no solids.The gas-solid suspension around the bubbles is defined as the emulsion phase (Figure 2.4a). The bubbles will rise due to the buoyancy force and increase in size with particle diameter d_p, excess gas velocity ($U - U_{mf}$) and with its distance above the grid of the bed. A bubble carrying particles in its wake bursts at the bed surface ejecting the particles into the freeboard section (Figure 2.4b) [7] [6].

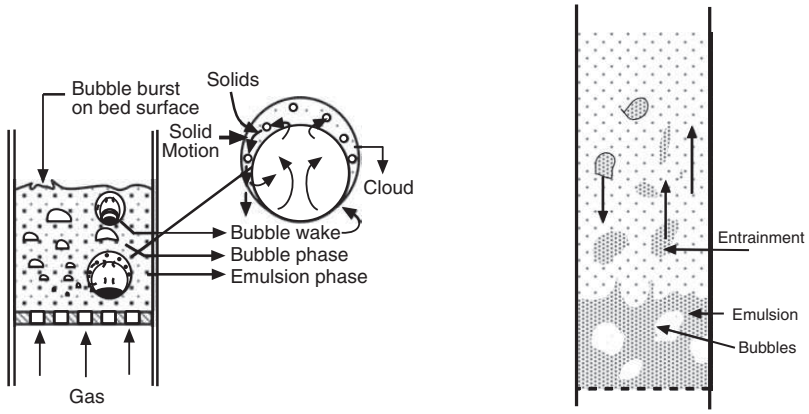

(a) Emulsion phase around a bubble.

(b) Bubble eruption ejecting particles.

Figure 2.4: Emulsion phase and ejection of particles in a BFB [7].

Most BFB gasifiers use group B particles, which results in large bubbles thus high bubble rise velocities.

2.2.1.3. SLUGGING

In case the bed is deep and has a small cross sectional area A_b, the bubbles may increase to a size comparable to the width of the bed (Figure 2.5). This is known as slugging and can cause a high unstable pressure drop fluctuation across the bed ($B-C$ trajectory in Figure 2.2). Commercialized fluidized bed gasifiers are generally too large in diameter to face the problems of slugging [7].

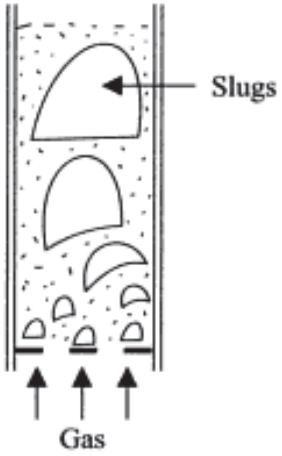

Figure 2.5: Slugging [6].

2.2.1.4. TURBULENT BED

With the gas flow velocity increasing even more, the bed expands and a point is reached where the emulsion walls separating the bubbles become very thin, the bubbles constantly collapse and re-form, resulting in a violently active highly expanded bed (Figure 2.6a).The pressure drop across the bed fluctuates rapidly until the velocity U reaches a peak velocity U_c and reduces to a steady state value U_k as seen in Figure 2.6b.

In the regimes so far, the solids are generally kept within the bed and there's no large migration of particles from the bed, except for some entertainment. These regimes are said to be in the captive stage [6].

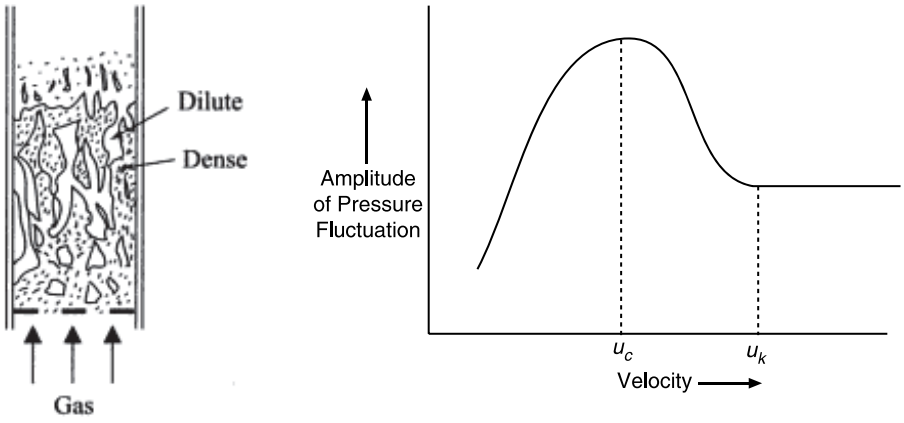

(a) Turbulent bed.

(b) Transition from bubbling to turbulent bed [7].

Figure 2.6: Turbulent bed behaviour [6].

2.2.1.5. FAST FLUIDIZED BED

At a high velocity gas–solid suspension, the particles are elutriated by the fluidizing gas (with a velocity higher than the terminal velocity of individual particles) and are recovered and returned to the base of the furnace at a sufficiently high rate to cause a degree of solid refluxing that will ensure a minimum level of temperature uniformity in the furnace. The term "fast bed" has become synonymous with the CFB. The entrained particles are carried away, thus the pressure drop decreases and will reach zero if all particles are carried away by the gas stream ($C-D$ trajectory in Figure 2.2) [6].

2.2.2. OVERVIEW GAS-SOLID PROCESSES

Table 2.2 gives an overview of the gas-solid contacting processes as mentioned in Basu [7].

Table 2.2: Comparison of Principal Gas – Solid Contacting Processes [13][7].

Property	*Packed Bed*	*Fluidized Bed*	*Fast bed*	*Pneumatic transport*
Application in boilers	Stoker fired	Bubbling fluidized	Circulating fluidized	Pulverized coal fired
Mean particle diameter (mm)	<300	0.03-3	0.05-0.5	0.02-0.08
Gas velocity through gasification zone (m/s)	1-3	0.5-3	3-12	15-30
Typical U/Ut	0.01	0.3	2	40
Gas motion	Up	Up	Up	Up & down
Gas mixing	Near plug flow	Complex two phases	Dispersed plug flow	Near plug flow
Solids motion	Static	Up & down	Mostly up, some down	Up
Solids-solids mixing	Neglible	Usually near perfect mixing	Near perfect mixing	Near plug flow
Overall voidage	0.4 - 0.5	0.5-0.85	0.85-0.99	0.98-0.998
Temperature gradient	Large	Very small	Small	May be significant
Typical bed-to-surface heat transfer coefficient (W/ m^2K)	50 -150	200-550	100-250	50-100
Attrition	Little	Some	Some	Considerable
Agglomeration	Considerable	Some	No problem	No problem

2.3. MECHANISMS OF HEAT TRANSFER

In a fluidized bed, several modes of heat transfer can be identified:

- Between the gas and particles.
- Between the bed and walls of a fast fluidized bed furnace.
- To the radiant tubes immersed in the BFB furnace.
- Between the freeboard and tubes.
- To the walls of cyclone or other primary separator.

This section will discuss different modes of heat transfer mainly occurring in a BFB gasifier, and presents some equations for the estimation of heat transfer coefficients.

In thermodynamics, heat is defined as the energy that crosses the boundary of a system when this energy transport occurs due to a temperature difference between the system and its surroundings. The second law of thermodynamics states that heat always flows over the boundary of the system in the direction of lower temperatures. In order to understand the types, driving force & the intensity of heat transfer, three mechanisms of heat transfer can be distinguished, conduction, convection, and radiation [24][25].

For BFBs, it is difficult to compute the heat transfer purely from the theory, so equations are developed based on many experiments. Mechanistic models are developed primarily for data extrapolation and qualitative understanding of the heat transfer process. One of the following two approaches can be used to calculate the heat transfer coefficient for a BFB.

- Based on mechanistic models or empirical equations.
- Based on design graphs

Heat transfer in a BFB is best explained by the packet-renewal model developed by Mickley and Fairbanks (1955). According to this model, packets of particles (or parcels of emulsion phase) at the bulk bed temperature are swept to the heat-transfer surface due to the action of bubbles. The packets stay in contact with the surface for a short time and are then swept back to the bed. During this time of contact, unsteady state heat transfer takes place between the packet and the surface. The first layer of particles, closest to the wall temperature (Figure 2.7a) is the most important layer for heat transfer. The first layer of particles in a fluidized bed is frequently replaced by fresh particles from the bulk of the bed (Figure 2.7b). New particles, being at bed temperature, increase the temperature differential with the wall resulting in a high heat-transfer coefficient. Thus, the particle renewal is the main driver of high heat-transfer coefficients in a fluidized bed. The bubbles sweeping over the surface are responsible for the particle renewal. The heat transfer between the tubes and the fluidized bed is made up of contributions of the bubble and the emulsion phase.

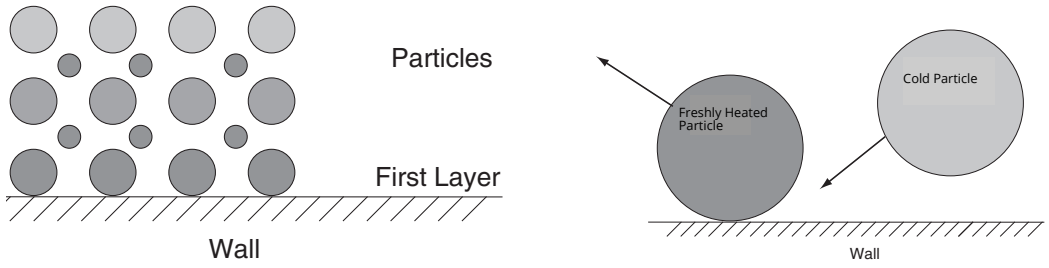

(a) Most important layer is the first or the layer adjacent to the wall.

(b) Particle replacement adjacent to surface in fluidized bed [7]

Figure 2.7: Packet-renewal model first layer[7]

2.3.1. HEAT CONDUCTION

Heat conduction is the transfer of energy between neighbouring molecules in a substance due to a temperature gradient. In fluids and gases, it is driven by collisions and diffusion of molecules. In metals, also the free electrons transfer energy. In solids which do not transmit radiation, heat conduction is the only process for energy transfer. The heat transfer rate due to conduction has been defined by Fourier's law as:

$$q_{conduction} = -k \cdot \nabla T, \tag{2.10}$$

where k is the thermal conductivity of the material and ∇T the temperature gradient [25].

In the case of a two-phase flow, like in a BFB, the total conductive heat flux can be written as

$$q_{cond} = -\left[\epsilon k_f + (1-\epsilon)\, k_s\right] \nabla T = -k_m \nabla T, \tag{2.11}$$

where k_f and k_s are effective conductive properties of the fluid and solid phase respectively and k_m is the mixture conductivity, also referred to as the effective bed conductivity k_b, which can be determined experimentally [26]. The model to determine the effective bed properties will be discussed in section 3.2.1.

2.3.2. CONVECTION

Convection is the transport of thermal energy, stored in particles or molecules within a fluid, caused by the fluid motion. Newton's law of cooling describes the convective heat transfer from a solid surface to its surroundings as:

$$\frac{\mathrm{d}}{\mathrm{d}t}\left(Q_{convection}\right) = h_{conv} A \left(T_s - T_\infty\right), \tag{2.12}$$

where h is the convective heat transfer coefficient, A is the surface area of the solid boundary, T_s the surface temperature of the solid body and T_∞ the temperature of the surrounding fluid far from the solid surface. The convective heat transfer coefficient can also be expressed in its dimensionless form as the Nusselt number Nu. The Nusselt number is the ratio of convective to conductive heat transfer across a boundary:

$$Nu = \frac{\text{Convective Heat Transfer}}{\text{Conductive Heat Transfer}} = \frac{hL}{k}, \tag{2.13}$$

where L is the characteristic length.

Convection itself can be divided into forced and natural convection, where forced convection is when the motion of the fluid is driven by external forces form e.g. fans or pumps. In natural convection, the fluid motion is driven by temperature differences in the domain, giving rise to density gradients.

2.3.3. THERMAL RADIATION

Thermal radiation comprises electromagnetic waves and is defined as the radiation energy that is emitted specifically because of the temperature of a medium or a body. Radiation can also be described as mass-less energy quanta, a photon. In the electromagnetic spectrum, thermal radiation covers part of the ultra violet, the visible, and part of the infrared spectrum and is found at wavelengths between 0.1-100 μm as seen in Figure 2.8 [27].

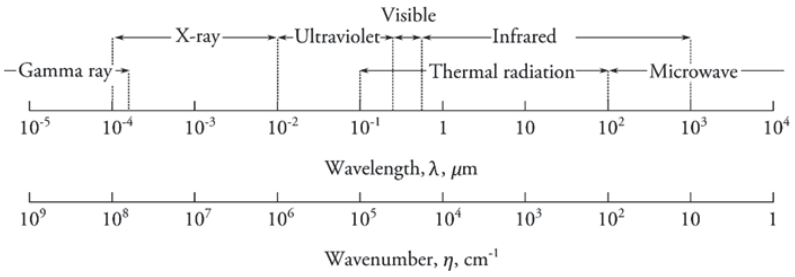

Figure 2.8: Common spectra within part of the electromagnetic spectrum.

Radiative heat transfer does not require any medium between the surfaces, as for convection and conduction. It does however require surfaces that can exchange radiative heat.

2.3.3.1. BLACK & GRAY BODY RADIATION

All bodies with a temperature above absolute zero emits radiation. The maximum radiation that can leave a body is blackbody radiation. A black body absorbs all radiation independent of incident direction and emits equally strong radiation in all directions. The spectral emissive power of a blackbody is given by Planck's law as:

$$E_{b\lambda} = \frac{2\pi h_P c_o^2}{n^2 \lambda^5 \left(e^{\frac{h_P c_o}{n k_b T}} - 1 \right)}, \tag{2.14}$$

where λ is the wavelength, n the refractive index. h_P the Planck constant, c_0 the speed of light, and k_B the Boltzmann constant.

Wien's displacement law states that the spectral radiance of black-body radiation per unit wavelength at a given temperature T, peaks at the wavelength λ_{max}:

$$\lambda_{max} = \frac{b}{T}, \tag{2.15}$$

where b is the Wien's displacement constant, equal to approximately 2900 μmK.

The higher the temperature of the blackbody, the higher the emissive power will be, as illustrated

in Figure 2.8 for a number of temperatures, and the maximum spectral emissive power tends towards lower wavelengths with increasing temperature of the blackbody.

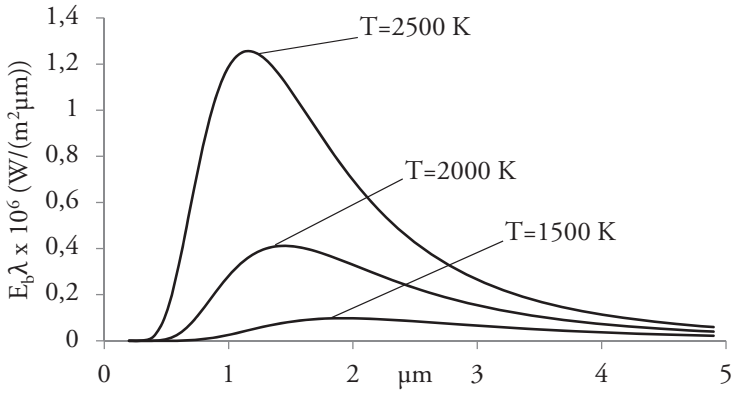

Figure 2.9: The blackbody emissive power at different temperatures [8].

The blackbody total emissive power is defined as:

$$E_b = \sigma T^4. \tag{2.16}$$

When the body partially absorbs incident electromagnetic radiation it is called a gray body. The ratio of a gray body's thermal radiation to a black body's thermal radiation at the same temperature is called the emissivity of the gray body:

$$e = \frac{E(T)}{E_b(T)}. \tag{2.17}$$

The net radiative heat transfer from a surface to its surroundings is calculated as

$$\frac{\mathrm{d}}{\mathrm{d}t}(Q_{radiation}) = e\sigma A\left(T_s^4 - T_{surr}^4\right). \tag{2.18}$$

2.3.3.2. INTERACTIONS WITH A SURFACE OR MEDIUM

Three distinct phenomena can occur for the incident radiation upon a surface: absorption, reflection and transmission. Absorptivity, α, reflectivity,ρ and the transmissivity τ are defined to describe the surface properties. Because of the conservation of energy the sum of the absorbed, reflected, and transmitted energy is always equal to the incident radiative energy such that $\alpha + \rho + \tau = 1$. A surface that is not transmitting any radiation is called an opaque surface, and the incident radiation is either absorbed or reflected, such that $\alpha + \rho = 1$ If the medium through which radiative energy travels is "participating," then any incident beam will be attenuated by absorption and scattering while it travels through the medium, as schematically shown in Figure 2.10.[9]

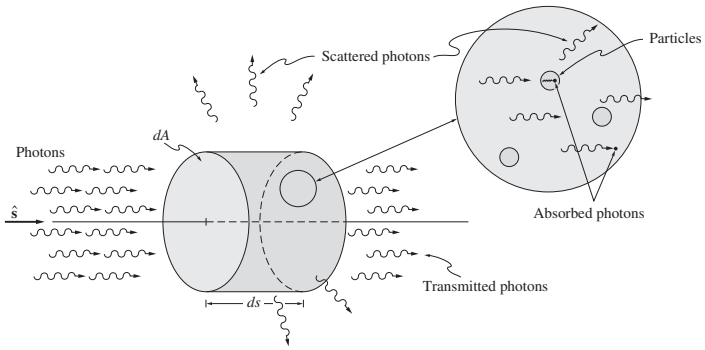

Figure 2.10: Attenuation of radiative intensity by absorption and scattering.[9]

The amount of the incident beam I that is absorbed is given by:

$$(dI)_{abs} = -aIds, \tag{2.19}$$

where a is the linear absorption coefficient. Attenuation by scattering is very similar to absorption as part of the incoming intensity is removed from the direction of propagation, $\hat{s}$. The difference being that the absorbed energy is converted into internal energy, while scattered energy is simply redirected and appears as augmentation along another direction, given by:

$$(dI)_{sca} = -\sigma_s Ids. \tag{2.20}$$

The total attenuation of the intensity by both absorption and scattering is known as extinction, where the extinction coefficient β_s is defined as:

$$\beta_s = a + \sigma_s. \tag{2.21}$$

The optical thickness τ is calculated based on the extinction as:

$$\tau = \int_0^s \beta_s ds. \tag{2.22}$$

When the optical thickness is high, the medium can be referred as optically thick. When the optical thickness is low the medium can be defined as optically thin. In case of an optically thick medium, only a small layer at the side where radiation enters is heated up and when the condition is optically thin, the radiation reaches the opposite side of the reactor.

The scattering behaviour depends on the material and size of the particles and can be defined by the scattering phase function $\Phi\left(\overrightarrow{s_i}, \overrightarrow{s}\right)$. The scattering phase function describes the probability that a ray from one direction, $\overrightarrow{s_i}$ will be scattered into a certain other direction $\overrightarrow{s}$ in the cone $d\Omega$ as seen in Figure 2.11a,

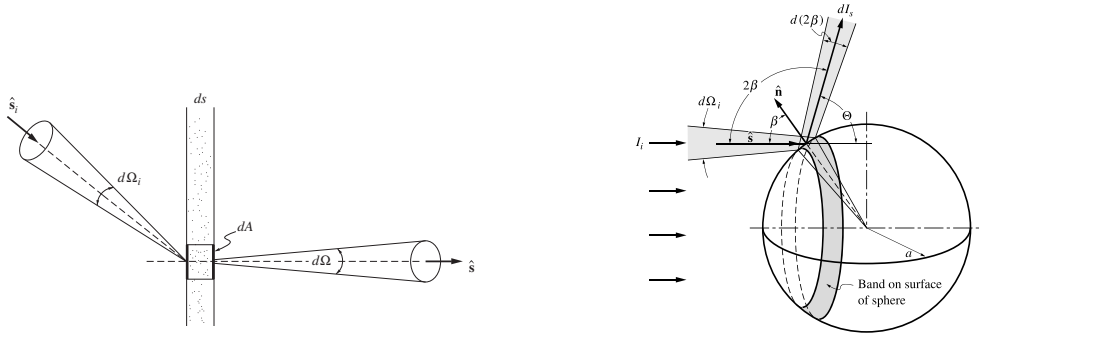

(a) Redirection of radiative intensity by scattering.

(b) Scattering of incident radiation by a large specularly reflecting sphere.

Figure 2.11: Radiation Scattering [9].

where the following holds true:

$$\frac{1}{4\pi}\int_{4\pi} \Phi\left(\overrightarrow{s_i}, \overrightarrow{s}\right) d\Omega = 1, \tag{2.23}$$

and the solid angle is given by:

$$d\Omega = 2\pi sin\left(2\beta\right) d\left(\beta\right), \tag{2.24}$$

where β is the angle between the incident ray and the normal of the surface as seen in Figure 2.11b.

2.3.3.3. RADIATIVE PROPERTIES OF PARTICULATE MEDIA

When the medium consists of small particles, as is the case of a fluidized bed, the radiative intensity may be changed by absorption and/or scattering. The radiative properties of a cloud of spherical particles of radius r, interacting with a wavelength λ, are governed by three independent nondimensional parameters:

$$\text{complex index of refraction: } m = n - ik, \tag{2.25a}$$

$$\text{size parameter: } x = 2\pi r/\lambda, \tag{2.25b}$$

$$\text{clearance to wavelength ratio: } c/\lambda. \tag{2.25c}$$

If scattering is independent ($c/\lambda >> 1$), only the complex index of refraction m and the size parameter x are relevant.

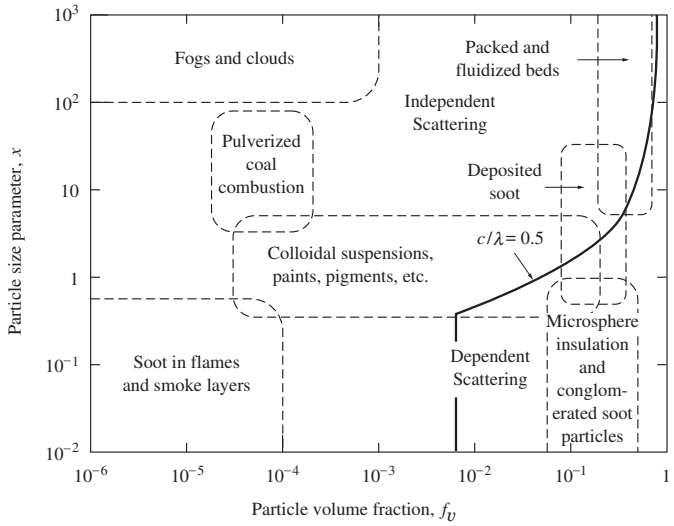

Figure 2.12: Scattering regime map for independent and dependent scattering[10]

According to Figure 2.12, in the case of fluidized beds, independent scattering can be assumed for solid volume fractions up to 0.7. If the scattering is independent, then the effect of large numbers of particles on the absorption and scattering is simply additive. For simplicity, it is assumed that particle clouds consist of spheres of uniform radius r. The absorption, scattering- and extinction coefficients are dependent on the number of particles per unit volume N_T which can be expressed as a function of the solid volume fraction α_s:

$$N_T = \frac{\alpha_s}{\frac{4}{3}\pi r^3}. \tag{2.26}$$

The absorption, scattering- and extinction coefficient for a cloud of uniform particles are then defined as:

$$a = \pi r^2 N_T Q_{abs} = \frac{3\alpha_s}{4r} Q_{abs}. \tag{2.27}$$

$$\sigma_s = \pi r^2 N_T Q_{scat} = \frac{3\alpha_s}{4r} Q_{scat}. \tag{2.28}$$

$$\beta = \sigma_s + a = \pi r^2 N_T Q_{ext} = \frac{3\alpha_s}{4r} Q_{ext}. \tag{2.29}$$

Q_{abs}, Q_{scat} and Q_{ext} are the absorption- scattering and extinction efficiency factors, and can be determined based on the optical properties of the particle cloud (equation 2.25a) and the size parameter x (equation 2.25b). Since the scattering phase function (or the directional distribution of scattered energy) in a cloud of uniform particles is the same for each particle, it is also the same for the particle cloud:

$$\Phi_T(\Theta) = \Phi(\Theta). \tag{2.30}$$

Three types of scattering can be distinguished:

- $x << 1$, or Rayleigh scattering, named after Lord Rayleigh, who studied the interaction of atmospheric air (whose molecules are, in fact, very small particles) with sunlight.
- $x \approx 1$, or Mie scattering, named after Gustav Mie, who developed a comprehensive theory for the interaction between electromagnetic waves and particles [28].
- $x >> 1$. In this case the surface of the particle may be treated as a normal surface, and properties may be found through geometric optics [9].

For fluidized beds, the particle size is much higher than the wavelengths of interest for heat transfer applications, thus the material properties are obtained through geometric optics. Also for heat transfer applications, diffraction is neglected, thus the extinction efficiency for large particles is:

$$Q_{ext} = 1. \tag{2.31}$$

For large, opaque specularly reflecting particles, the scattering and absorption efficiency are defined as:

$$Q_{scat} = \rho^s. \tag{2.32a}$$

$$Q_{abs} = Q_{ext} - Q_{scat} = 1 - \rho^s = \alpha^s, \tag{2.32b}$$

where α^s and ρ^s are the hemispherical absorptivity and reflectivity of a sphere. If the particle behaves like a dielectric as is assumed to be the case for corundum, ($k \ll n$ in equation 2.25a), the hemispherical absorptivity is equal to its hemispherical emmisivity e_λ, which is derived by Dunkle [29] as:

$$e_{||} = \frac{4\,(2n+1)}{3\,(n+1)^2}, \tag{2.33a}$$

$$e_\perp = \frac{4n^3\left(n^2+2n-1\right)}{\left(n^2+1\right)\left(n^4-1\right)} + \frac{2n^2\left(n^2-1\right)^2}{\left(n^2+1\right)^3}\ln\left(\frac{n+1}{n-1}\right) - \frac{16n^4\left(n^4+1\right)\ln n}{\left(n^2+1\right)\left(n^4-1\right)^2}, \tag{2.33b}$$

$$e_\lambda = \frac{1}{2}\left(e_{||} + e_\perp\right). \tag{2.33c}$$

For a cloud of dielectric particles, there is stronger forward scattering than back scattering, as mentioned in Modest [9].

3

MULTIPHASE MODELLING OF A FLUIDIZED BED

In the past, the modelling of the hydrodynamic behaviour in a bubbling fluidized bed was approached mostly by experimental measurements and analytical analysis, rather than numerical simulation due to huge computation time needed and the lack of validation methods. With advancements in technology, the computation time has been much reduced, making numerical analysis such as CFD (computational fluid dynamics) one of the more attractive techniques to predict the flow behaviour in a fluidized bed. This chapter provides more insight into the models developed and best suited to predict the hydrodynamics of a bubbling fluidized bed.

3.1. MODELLING THE HYDRODYNAMICS OF A FLUIDIZED BED

3.1.1. HISTORY OF MODELLING FLUIDIZED BED SYSTEMS

Several modelling approaches were developed to study the hydrodynamic behaviour of fluidized bed systems. The fundamental understanding of fluidization was reported by Davidson and Harrison [30] who analysed the single bubble motion in an infinite fluidized bed.
Rhodes and Geldart [31] used a semi-emperical model based on entrainment and expansion bed correlations to predict axial and radial non homogeneous particle distribution in a CFB.
Tsuo and Gidaspow [32] simulated the cluster formation and predicted the core-annulus model of particle by using a two dimensional transient two phase flow model.

A model based on constant viscosity for the solid phase was researched and found to be applicable to both a BFB as reported by Lyczkowsky *et al.* [33] and Anderson *et al.* [34] and a CFB as reported by Benyahia *et al.* [35]) and Sun and Gidaspow [36].

The investigation on gas-solid flow systems became more attractive with the development of kinetic theory for gas-solids two-phase flow based on the theory of non-uniform dense gases described by Champan and Cowling [37]. Lun *et al.* [38] applied the kinetic theory of gases to granular flow. The kinetic theory approach used a one equation model to determine the turbulent kinetic energy of the particles (expressed in granular temperature) and assumed either a Maxwellian or a non-Maxwellian distribution of particles for both dilute and dense cases. The kinetic theory approach for granular flow allows the determination of the pressure and viscosity of the solids in terms of empirical relations. Sinclair and Jackson [39] applied the granular flow model to a fully developed gas-solids flow in a pipe.

Ding and Gidaspow [32] derived expressions for solids viscosity and pressure of a dense gas-solids flow. Gidaspow [40] expanded the Ding and Gidaspow formulation to be valid for both dilute and dense phase conditions by considering a non-Maxwellian velocity distribution. Nieuwland *et al.* [41], Balzer *et al.* [42] and Neri and Gidaspow [43] conducted simulations of gas-solids flow in the circulating fluidized bed using the kinetic theory of granular flow.

With CFD, two-fluid models (TFM) for the numerical calculation of multiphase flows have been developed: the Euler-Lagrange approach and the Euler-Euler approach. Chiesa *et al.* [44] presented a computational study of the flow behavior of a lab-scale fluidized bed where the experimental results

of a two-dimensional lab-scale bubbling fluidized bed were compared to their computational results. The results showed, when Eulerian and Lagrangian approaches were applied, the numerical simulations led to a rather similar pattern compared to the experimental data.

In the Euler-Euler approach, the different phases are treated mathematically as interpenetrating continua. Since the volume of a phase cannot be occupied by the other phases, the concept of phase volume fraction is introduced. These volume fractions are assumed to be continuous functions of space and time and their sum is equal to one. Conservation equations for each phase are derived to obtain a set of equations, which have similar structure for all phases. These equations are closed by providing constitutive relations that are obtained from empirical information or in the case of granular flows, by application of kinetic theory [11].

In the Euler-Lagrange approach, the fluid phase is treated as a continuum by solving the Navier-Stokes equations, while the dispersed phase is solved by tracking a number of particles, bubbles, or droplets through the calculated flow field. The dispersed phase can exchange momentum, mass, and energy with the fluid phase. The particle or droplet trajectories are computed individually at specified intervals during the fluid phase calculation. A fundamental assumption made in this model is that the dispersed second phase occupies a low volume fraction, even though high mass loading ($\dot{m}_{particles} \geq \dot{m}_{fluid}$) is acceptable. Due to calculating the trajectory for every individual particle, it would be computationally intensive to model fluidized bed behaviour compared to the Euler-Euler approach ,as the volume fraction of the second phase is not negligible in a fluidized bed [11].

The Euler-Euler approach is less computationally extensive and is therefore considered in this work.

3.1.2. THE EULER- EULER APPROACH

In ANSYS® FLUENT, three different Euler-Euler multiphase models are available: the volume of fluid (VOF) model, the mixture model, and the Eulerian model.

The VOF model is designed for two or more immiscible fluids where the position of the interface between the fluids is of interest. In the VOF model, a single set of momentum equations is shared by the fluids, and the volume fraction of each of the fluids in each computational cell is tracked throughout the domain. Applications of the VOF model include stratified flows, free-surface flows, filling, sloshing, the motion of large bubbles in a liquid, the motion of liquid after a dam break, the prediction of jet breakup (surface tension), and the steady or transient tracking of any liquid-gas interface [11].

The mixture model is designed for two or more phases (fluid or particulate). The phases are treated as interpenetrating continua. The mixture model solves the momentum equation and prescribes relative velocities to describe the dispersed phases. Applications of the mixture model include particle-laden flows with low loading, bubbly flows, sedimentation , and cyclone separators. The mixture model can also be used without relative velocities for the dispersed phases to model homogeneous multiphase flow [11].

The Eulerian model is the most complex of the multiphase models in ANSYS® Fluent. It solves a set of n momentum and continuity equations for each phase. Coupling is achieved through the pressure and inter-phase exchange coefficients. The manner in which this coupling is handled depends upon the type of phases involved; granular (fluid-solid) flows are handled differently than nongranular (fluid-fluid) flows. For granular flows, the properties are obtained from application of kinetic theory. Momentum exchange between the phases is also dependent upon the type of mixture being modeled. Applications of the Eulerian multiphase model include bubble columns, risers, particle suspension, and fluidized beds [11].

Based on the description, the Eulerian model is chosen to model the fluidized bed, ANSYS® Fluent Eulerian multiphase model does not distinguish between fluid-fluid and fluid-solid (granular) multiphase flows. A granular flow is simply one that involves at least one phase that has been designated as a granular phase.

The ANSYS® Fluent solution is based on the following:

- A single pressure is shared by all phases.
- Momentum and continuity equations are solved for each phase.
- The following parameters are available for granular phases:
  - Granular temperature (solids fluctuating energy) can be calculated for each solid phase.
  - Solid-phase shear and bulk viscosity's are obtained by applying kinetic theory to granular flows. Frictional viscosity for modelling granular flow is also available. This will be explained in more detail in section 3.1.4
- Several inter-phase drag coefficient functions are available, which are appropriate for various types of multiphase regimes and influence the hydrodynamic behaviour of a fluidized bed.

3.1.2.1. CONTINUITY EQUATIONS

The principle of general mass conservation or the continuity equations is based on that fact that all the mass flow rates into the control volume (CV) are equal to the sum of all mass flow rates out of the CV and the rate of change of mass within the CV. This can be applied to individual flow components as well to the overall flow stream. The mass conversion equations or the continuity equations for gas and solid flows in fluidized beds according to Gibilaro [45] and Papadikis *et al.* [46] are given below,

for the gas phase:

$$\frac{\partial}{\partial t}(\alpha_g \rho_g) + \nabla.(\alpha_g \rho_g \overrightarrow{v}_g) = 0. \tag{3.1a}$$

for the solid phase:

$$\frac{\partial}{\partial t}(\alpha_s \rho_s) + \nabla.(\alpha_s \rho_s \overrightarrow{v}_s) = 0. \tag{3.1b}$$

where ρ_g, ρ_s, stand for density, $\overrightarrow{v}_g, \overrightarrow{v}_s$ the velocity and α_g, α_s for the volume fraction of the gas and solid phase respectively. It is assumed there is no inter-species mass transfer occurring between the two phases. The phases are able to interpenetrate and the sum of all volume fractions in each computational cell is equal to one:

$$\alpha_f + \alpha_s = 1, \tag{3.2}$$

3.1.2.2. MOMENTUM EQUATIONS

Momentum is a vector quantity that possesses the directional properties of the phases and the corresponding magnitude involved in the CV. Like the mass conservation, momentum can also be conserved in the CV. The conservation of momentum of flows is defined by Newton's second law of motion in the fluidized bed. The momentum conservation equations are established according to Gibilaro [45] by considering the forces that act on the fluid mass of the system, the momentum carried into and out of the systems. In this case, there is no lift force (particles are too small in size for the lift force to be significant) and virtual mass force (only significant when $\rho_s \ll \rho_g$). Thus only the drag and buoyancy forces are taken into account. In addition, the inter-phase momentum transfer term β is also included in the momentum conservation equation based on Navier-Stokes equations [46]. The momentum equations are given as follows,

for the gas phase:

$$\frac{\partial}{\partial t}(\alpha_g \rho_g \overrightarrow{v}_g) + \nabla(\alpha_g \rho_g \overrightarrow{v}_g \overrightarrow{v}_g) = -\alpha_g \nabla P_g + \alpha_g \rho_g g + \beta(\overrightarrow{v}_g - \overrightarrow{v}_s) + \nabla \overrightarrow{\sigma}_s, \tag{3.3a}$$

and for the solid phase:

$$\frac{\partial}{\partial t}(\alpha_s \rho_s \overrightarrow{v}_s) + \nabla(\alpha_s \rho_s \overrightarrow{v}_s \overrightarrow{v}_s) = -\alpha_s \nabla P_s + \alpha_s \rho_s g + \beta(\overrightarrow{v}_s - \overrightarrow{v}_g) + \nabla \overrightarrow{\sigma}_s. \tag{3.3b}$$

The terms on the right-hand side of momentum equations (3.3a & 3.3b) are respectively the pressure drop, gravity, fluid particulate inter-phase drag forces and the phase viscous stress tensors. P_g and P_s are the gas and solid pressure, β is the particulate inter-phase drag coefficient, $\overrightarrow{\sigma}_g$ and $\overrightarrow{\sigma}_s$ the viscous stress tensors that are obtained from the basic fluid field variables. The viscous stress tensor for the gas phase is given by:

$$\overrightarrow{\sigma}_g = 2\alpha_g \mu_g \overrightarrow{\tau}_g, \tag{3.4a}$$

and for the solid phase:

$$\overrightarrow{\sigma}_s = (\xi_s \nabla v_s) I + 2\alpha_s \mu_s \overrightarrow{\tau}_s, \tag{3.4b}$$

The tensor $\overrightarrow{\tau}_i$ (i= g, s) for the gas and solid phase is defined by Papadikis *et al.* [46] as:

$$\overrightarrow{\tau}_i = \frac{1}{2}\left[\nabla \overrightarrow{v}_i + \left(\nabla \overrightarrow{v}_i\right)^T\right] - \frac{1}{3}\left(\nabla \overrightarrow{v}_i\right) I. \tag{3.5}$$

In order to solve the above model, the fluid particulate inter-phase drag coefficient (β), the solid bulk viscosity (ξ_s) and the solid shear viscosity (μ_s) need to be determined first and this will be discussed in section 3.1.3 and 3.1.4.

3.1.3. FLUID PARTICULATE INTER-PHASE DRAG COEFFICIENTS

In the solid-gas flow, gravity and drag are reported to be the dominant forces for the majority of flows with granular particles as the solid phase. For very dense flows, the frictional stresses became more important. For relatively small particles with densities being much larger than the density of the continuous gas phase, the fluid particulate inter-phase drag force is dominant over the other forces such as lift and virtual mass (Ranade, 2002). Wen and Yu (1966) modelled the fluid particulate drag coefficient which was only valid for dilute systems. Gidaspow *et al.* [47] combined the Ergun equation coefficients with the model of Wen and Yu for the fluid inter-phase drag coefficient which is applicable to dense fluidized beds. Syamlal and O'Brien [48] developed a drag model based on the correlation between the drag of a sphere and a multiparticle system and has a wider range of application. When modelling a CFB gasifier, the coefficient model developed by Gidaspow *et al.* [47] shows higher errors compared to a solid shear stress model proposed by Syamlal and O'Brien [48] which arises from particle momentum exchange due to collision. The particulate inter-phase drag coefficient developed by Gidaspow *et al.* [47] is given as:

$$\beta = \begin{cases} \frac{3}{4} C_d \frac{\alpha_s \alpha_g \rho_g |\overrightarrow{v}_s - \overrightarrow{v}_g|}{d_p} \alpha_g^{-2.65} & \text{for } \alpha_g > 0.8. \\ 150 \frac{\alpha_s^2 \mu_g}{\alpha_g^2 d_p^2} + 1.75 \frac{\alpha_s \rho_g |\overrightarrow{v}_s - \overrightarrow{v}_g|}{\alpha_g d_p} & \text{for } \alpha_g < 0.8. \end{cases} \tag{3.6}$$

where C_d is calculated as:

$$C_d = \begin{cases} \frac{24}{Re_s}\left[1 + 0.15\,(Re_s)^{0.687}\right] & \text{for } Re_s \leq 1000. \\ 0.44 & \text{for } Re_s > 1000. \end{cases} \tag{3.7}$$

and Re_s is the relative Reynolds number between the gas and solid phase calculated as:

$$Re_s = \frac{\alpha_g \rho_g |\overrightarrow{v}_s - \overrightarrow{v}_g| d_p}{\mu_g}. \tag{3.8}$$

The particulate inter-phase drag coefficient developed by Syamlal and O'Brien [48] is given by:

$$\beta = \frac{3}{4} \frac{\alpha_s \alpha_g \rho_g}{v_{r,s}^2 d_s} C_d \left(\frac{Re_s}{v_{r,s}}\right) |\overrightarrow{v}_s - \overrightarrow{v}_g|. \tag{3.9}$$

In this case, the drag coefficient C_d is derived by Valle [49] and is determined from the relative Reynolds number Re_s and the terminal velocity for the solid phase $v_{r,s}$.

$$C_d = \left(0.63 + \frac{4.8}{\sqrt{Re_s / v_{r,s}}}\right)^2. \tag{3.10}$$

The terminal velocity for the solid phase is given as:

$$v_{r,s} = 0.5\left(A - 0.06Re_s + \sqrt{(0.06Re_s)^2 + 0.12Re_s(2B - A) + A^2}\right), \tag{3.11}$$

where $A = \alpha_g^{4.14}$ and $B = \begin{cases} 0.8\alpha_g^{1.28} & \text{for } \alpha_g \leq 0.85. \\ \alpha_g^{2.65} & \text{for } \alpha_g > 0.85. \end{cases}$

3.1.4. KINETIC THEORY OF GRANULAR FLOW (KTGF)

The KTGF was developed to model the fluctuation of solid velocity and its variations due to gas flow causing the particles to impact one another [38]. All the granular phase properties, such as the solids pressure, the solids shear stress, the solids shear viscosity and the solid bulk viscosity are expressed in terms of the granular temperature. The granular temperature for the solids phase is proportional to the kinetic energy of the particles's random motion:

$$\Theta_s = \frac{1}{3}\vec{v_s} \cdot \vec{v_s} \tag{3.12}$$

In this approach, the average kinetic energy, represented by granular temperature of the solid phase (Θ_s), is computed by solving the transport equation of the KTGF for the randomly moving particles given as:

$$\frac{3}{2}\left[\frac{\partial}{\partial t}\left(\alpha_s \rho_s \Theta_s\right) + \nabla\left(\alpha_s \rho_s \vec{v}_s \Theta_s\right)\right] = \vec{\sigma}_s : \nabla \vec{v}_s + \nabla(\kappa_s \nabla \Theta_s) - \gamma_s. \tag{3.13}$$

The first term on the right-hand side is the production of fluctuating energy by the effective solid shear stresses. The second term is the diffusive flux of granular energy due to the gradient of granular temperature with κ_s describing the diffusion coefficient. The third term is the dissipation energy due to the inelastic collisions between particles γ_s. In order to solve the fluctuating energy equation, γ_s and κ_s need to be determined.

κ_s has been derived by Syamlal *et al.* [50] as follows:

$$\kappa_s = \frac{15 d_p \alpha_s \rho_s \sqrt{\Theta_s \pi}}{4\left(41 - 33\eta\right)}\left[1 + \frac{12}{5}\eta^2\left(4\eta - 3\right) g_o \alpha_s + \frac{16}{15\pi}\left(41 - 33\eta\right)\eta g_o \alpha_s\right], \tag{3.14}$$

where $\eta = \frac{1}{2}(1 + e_{ss})$, Θ_s is the granular temperature, g_0 is the radial distribution function and e_{ss} is the restitution coefficient of particles.

γ_s is derived by Lun *et al.* [38] as follows:

$$\gamma_s = \frac{12\left(1 - e_{ss}^2\right) g_0}{d_p \sqrt{\pi}} \rho_s \alpha_s^2 \Theta_s^{3/2}. \tag{3.15}$$

The radial distribution function g_0 is a correction factor that modifies the probability of collisions between particles when the solid granular phase becomes dense. It is a function that governs the transition from the "compressible" condition with $\alpha_s < \alpha_{s,max}$, where the spacing between the solid particles can continue to decrease, to the "incompressible" condition with $\alpha_s = \alpha_{s,max}$ where no further decrease in the spacing can occur.

g_0 is given by Ogawa *et al.* [51] as:

$$g_0 = \left[1 - \left(\frac{\alpha_s}{\alpha_{s,max}}\right)^{1/3}\right]^{-1}, \tag{3.16}$$

where it is assumed there is no more than one solid phase.

The restitution coefficient e_{ss} compensates for the collisions to be inelastic. In a completely elastic

collision the restitution coefficient will be one.

Once the granular temperature is known, the solid pressure and its gradient, the solid shear viscosity and solid bulk viscosity can then be computed as a function of granular temperature at any time and position. For granular flows in the compressible regime (that is, where the solids volume fraction is less than its maximum allowed value), a solids pressure P_s is calculated independently and used for the pressure gradient term ∇P in the granular-phase momentum equation, derived by Lun *et al.* [38] as:

$$P_s = \alpha_s \rho_s \Theta_s + 2\rho_s (1+e_{ss}) \alpha_s^2 g_0 \Theta_s. \tag{3.17}$$

The first term of the solids pressure is the kinetic term and the second term is due to particle collisions.

The granular viscosity is a summation of three viscosity contributions: the collisional $\mu_{s,col}$, kinetic $\mu_{s,kin}$ and frictional viscosity's $\mu_{s,fr}$ given by:

$$\mu_s = \mu_{s,col} + \mu_{s,kin} + \mu_{s,fr}. \tag{3.18}$$

The collisional viscosity is a viscosity contribution due to collisions between particles taken from the kinetic theory of granular flow of Lun *et al.* [38] given by:

$$\mu_{s,col} = \frac{4}{5} \alpha_s \rho_s g_0 (1+e_{ss}) \sqrt{\frac{\Theta_s}{\pi}}. \tag{3.19}$$

Both Gidaspow [40] and Syamlal *et al.* [50] derived expressions for the kinetic viscosity. The model for kinetic viscosity by Syamlal *et al.* [50] is based on the modified kinetic theory for smooth, inelastic spherical particles by Lun *et al.* [38]. This model assumes that the kinetic contribution to the viscosity is neglectable in the dilute region and is given by:

$$\mu_{s,kin} = \frac{\alpha_s d_p \rho_s \sqrt{\Theta_s \pi}}{6(3-e_{ss})} \left[1 + \frac{2}{3} (1+e_{ss})(3e_{ss}-1) \alpha_s g_0 \right]. \tag{3.20}$$

The model of kinetic viscosity by Gidaspow [40] is an extension of the kinetic theory given by:

$$\mu_{s,kin} = \frac{10 \rho_d f_p \sqrt{\Theta_s \pi}}{96 \alpha_s (1+e_{ss}) g_0} \left[1 + \frac{4}{5} g_0 \alpha_s (1+e_{ss}) \right]^2. \tag{3.21}$$

It is assumed here that a molecule is hard spherical particle. It is also assumed that the particles in the dilute region, like a molecule in low pressures, do not collide. Both the restitution coefficient and radial distribution function equal one.

The frictional viscosity accounts for the viscous-plastic transition that occurs when particles of a solid phase reach the maximum solid volume fraction. ANSYS® Fluent uses the model proposed by Schaeffer [52]. Due to the high computational effort to calculate this value, the frictional viscosity has been neglected in the modelling of the IH-BFBSR.

The solid bulk viscosity is the resistance the granular particles have to compression and expansion and is derived by Lun *et al.* [38] as:

$$\xi_s = \frac{4}{3} \alpha_s^2 \rho_s d_p (1+e_{ss}) g_0 \sqrt{\frac{\Theta_s}{\pi}}. \tag{3.22}$$

3.2. MODELLING THE HEAT TRANSFER OF A FLUIDIZED BED

In order to calculate the heat transfer, the conservation of energy equation needs to be solved. To describe the conservation of energy in Eulerian multiphase applications, a separate enthalpy equation can be written.

For the gas phase:

$$\frac{\partial}{\partial t}(\alpha_g \rho_g h_g) + \nabla.(\alpha_g \rho_g \vec{v}_g h_g) = \alpha_g \frac{\partial P_g}{\partial t} + \vec{\tau}_g : \nabla \vec{v}_g - \nabla \cdot \vec{q}_g + S + Q_{gs}. \tag{3.23a}$$

For the solid phase:

$$\frac{\partial}{\partial t}(\alpha_s \rho_s h_s) + \nabla.(\alpha_s \rho_s \vec{v}_s h_s) = \alpha_s \frac{\partial P_s}{\partial t} + \vec{\tau}_s : \nabla \vec{v}_s - \nabla \cdot \vec{q}_s + S + Q_{sg}, \tag{3.23b}$$

where h_g,h_s is the the specific enthalpy and q_g, q_s the conductive heat flux for the gas and solid phase, respectively. The first two terms on the right side are describing the work of expansion of void space and the viscous dissipation. S is a source term that includes sources of enthalpy (for example, due to chemical reactions or radiation), and Q_{gs} is the intensity of heat exchange between the gas- and solid phase. The heat exchange between phases must comply with the local balance conditions $Q_{gs} = -Q_{sg}$. The specific enthalpy h_i (i=g,s) is calculated as follows:

$$h_i = \int_{T_{ref}}^{T} C_{p,i}\, dT, \tag{3.24}$$

where $C_{p,i}$ is the specific heat at constant pressure of the gas/solid phase. The heat exchange between phases Q_{gs} can be expressed as a function of the temperature difference in consistency with the local balance conditions [17], as follows:

$$Q_{gs} = h_{gs}\left(T_g - T_s\right), \tag{3.25}$$

where h_{gs} is the heat transfer coefficient between the phases related to the Nusselt number of the solid phase given by:

$$h_{gs} = \frac{6 k_g \alpha_s \alpha_g Nu_s}{d_p^2}. \tag{3.26}$$

For a system of granular flow, the correlation of the Nusselt number Nu_s, is given by Gunn [53], suitable for a void fraction of the bed ranging from 0.35- 0.65 and a Reynolds number (equation 3.8) up to 10^5.

$$Nu_s = \left(7 - 10\alpha_g + 5\alpha_g^2\right)\left(1 + 0.7 Re_s^{0.2} Pr^{1/3}\right) + \left(1.33 - 2.4\alpha_g + 1.2\alpha_g^2\right) Re_s^{0.7} Pr^{1/3}, \tag{3.27a}$$

where

$$Pr = \frac{C_{p,g}\mu_g}{k_{g,o}}. \tag{3.27b}$$

3.2.1. EFFECTIVE THERMAL CONDUCTIVITY

The proper specification of the constitutive equations for the thermal conductivities k_g and k_s mentioned in section 2.3.2, poses a major difficulty in the theoretical formulation. In terms of the TFM approach, k_g and k_s must both be interpreted as effective transport properties which means that the corresponding microscopic transport coefficients $k_{g,o}$ and $k_{s,o}$ cannot be used. Both k_g and k_s are expected to depend on the voidage ϵ, $k_{g,o}$ and $k_{s,o}$ and the particle geometry, where the functional dependency must be specified partly by comparing to experimental data [26].

Equation 2.11 shows that Fourier's law of heat conduction has been used to represent the conductive heat transport in both phases. Zehner and Schlünder [54] obtained an approximate expression for the effective thermal bed conductivity k_b. This conductivity model was originally developed for the estimation of the effective radial thermal conductivity in packed beds. However, it can also be applied to estimate the effective dense phase thermal conductivity in fluidized beds [55].

According to the Zehner and Schlunder model, the radial bed conductivity k_b consists of a contribution $k_{b,f}$ due only to the fluid phase and a contribution $k_{b,s}$, due to a combination of the fluid phase and the solid phase given as:

$$k_b = k_{b,f} + k_{b,s}, \tag{3.28a}$$

where

$$k_{b,f} = \left(1 - \sqrt{(1-\epsilon)}\right) k_{f,o}, \tag{3.28b}$$

and

$$k_{b,s} = \sqrt{(1-\epsilon)}\,[\omega A + (1-\omega)\,C]\,k_{f,o}. \tag{3.28c}$$

Here ω is equal to $7.26{\cdot}10^{-3}$ and C is given by:

$$C = \frac{2}{1-\frac{A}{B}}\left[\frac{A-1}{\left(1-\frac{B}{A}\right)^2}\frac{B}{A}ln\frac{A}{B} - \frac{B-1}{\left(1-\frac{B}{A}\right)} - 0.5\,(B+1)\right], \tag{3.28d}$$

where for spherical particles,

$$A = \frac{k_{s,o}}{k_{g,o}}, \tag{3.28e}$$

and

$$B = 1.25\left(\frac{1-\epsilon}{\epsilon}\right)^{10/9}. \tag{3.28f}$$

Comparing equation 3.28a with equation 2.11, the desired constitutive equations for k_g and k_s, can finally be obtained:

$$k_g = \frac{k_{b,g}}{\epsilon}. \tag{3.29a}$$

$$k_s = \frac{k_{b,s}}{(1-\epsilon)}. \tag{3.29b}$$

3.2.2. MODELLING RADIATION

In ANSYS® Fluent, five radiation models are available that allow radiation, with or without a participating medium in heat transfer simulations.

- Discrete Transfer Radiation Model (DTRM) [56].
- P-1 Radiation Model [57].
- Rosseland Radiation Model [58].
- Surface-to-Surface (S2S) Radiation Model [58].
- Discrete Ordinates (DO) Radiation Model [59].

The DTRM is a relatively simple model, that neglects the effect of scattering, and it applies to a wide range of optical thicknesses. However the DTRM does not support parallel processing in ANSYS® Fluent which is recommended to reduce the computation time for multiphase flows.

The P-1 model simplifies the radiative transfer equation (RTE) to a diffusion equation, which is easy to solve with little CPU demand. The model includes the effect of scattering. For combustion applications where the optical thickness is large, the P-1 model works reasonably well. In addition, the P-1 model can easily be applied to complicated geometries with curvilinear coordinates. However, the implementation is restricted to either gray radiation or non-gray radiation using a gray-band model. The P-1 model tends to over-predict radiative fluxes from localized heat sources or sinks.

The Rosseland model is faster than the P-1 model and requires less memory, however can be used only for optically thick media.

The DO model spans the entire range of optical thicknesses, and allows you to solve problems ranging from surface-to-surface radiation to participating radiation in combustion problems. It also allows the solution of radiation at semi-transparent walls. Computational cost is moderate for typical angular discretizations, and memory requirements are modest. The current implementation is restricted to either gray radiation or non-gray radiation using a grayband model.

The surface-to-surface (S2S) radiation model is good for modelling the enclosure radiative transfer without participating media (for example, spacecraft heat rejection systems, solar collector systems, radiative space heaters, and automotive underhood cooling systems). In such cases, the methods for participating radiation may not always be efficient.

Based on the description either the P-1 model or the DO model seem suitable for modelling radiation in a fluidized bed. The DO-model is chosen for the modelling of the IH-BFBSR. A gray model is chosen, meaning that the absorption- and scattering coefficient are assumed to be independent of the wavelength.

3.2.2.1. DISCRETE ORDINATES (DO) RADIATION MODEL THEORY

The DO model considers the radiative transfer equation (RTE) at the position $\vec{r}$, in the direction $\vec{s}$, as a field equation, and is written as:

$$\nabla \cdot \left(I\left(\vec{r}, \vec{s}\right) \vec{s} \right) + (a + \sigma_s) I\left(\vec{r}, \vec{s}\right) = an^2 \frac{\sigma T^4}{\pi} + \frac{\sigma_s}{4\pi} \int_0^{4\pi} I\left(\vec{r}, \vec{s_i}\right) \Phi\left(\vec{s_i}, \vec{s}\right) d\Omega'. \tag{3.30}$$

The DO radiation model is solved for the mixture material, meaning that the radiative properties, such as the absorption coefficient a, refractive index n, and scattering coefficients σ_s of the mixture, are computed by volume fraction based averaging of the radiative properties of the individual phases, and are given as:

$$a = a_{mix} = \alpha_g a_g + \alpha_s a_s. \tag{3.31a}$$

$$\sigma_s = \sigma_{mix} = \alpha_g \sigma_{s,g} + \alpha_s \sigma_{s,s}. \tag{3.31b}$$

$$n = n_{mix} = \alpha_g n_g + \alpha_s n_s. \tag{3.31c}$$

The DO implementation in ANSYS® Fluent admits a variety of scattering phase functions: an isotropic phase function, a linear anisotropic phase function, a Delta-Eddington phase function, or a user-defined phase function. The linear anisotropic phase function will be used and is given as:

$$\Phi\left(\vec{s_i}, \vec{s}\right) = 1 + C\, \vec{s_i} \cdot \vec{s}\,. \tag{3.32}$$

The value of C ranges from –1 to 1. A positive value indicates that more radiant energy is scattered forward than backward, and a negative value means that more radiant energy is scattered backward than forward. If C is zero, linear anisotropic phase function simplifies to the isotropic phase function where it is assumed scattering is equally likely in all directions [11].

Applying the DO model, each octant of the angular space at any spatial location is discretized into $N_\theta \times N_\phi$ solid angles called control angles. The angles θ and ϕ are the polar and azimuthal angles respectively, and can be seen in Figure 3.1 . In two-dimensional calculations, only four octants are solved due to symmetry, making a total of $4N_\theta N_\phi$ directions.

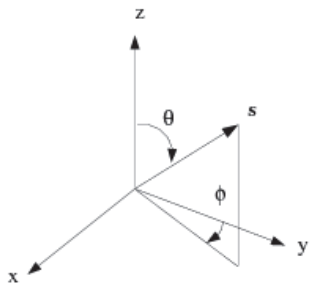

Figure 3.1: Angular Coordinate System[11]

3.3. COMPUTATIONAL STUDIES FOR A BFB

With the models suitable for multiphase flows in BFB being discussed, the next part of the research is finding parameters of interest that give insight into the hydrodynamical and heat transfer behaviour. Table 3.1 provides a list of research papers and an overview of the parameters that have been investigated, which have been used as a reference for approximating the scope of this research.

3.3.1. LITERATURE AND PARAMETER OVERVIEW

A comparison of the Gidaspow and Syamlal-O Brien drag models is pretty common in the study of the hydrodynamics of fluidized beds, as these drag models are already implemented into commercial CFD software like ANSYS® FLUENT. According to Taghipour *et al.* [60], the Gidaspow model and Syamlal-O Brien show similar trends to the experimental results (e.g. bed expansion ratio, pressure drop).

In regards to turbulence modelling, Chanchal [61] claims that there is no big difference in the hydrodynamic behaviour, and suggest that unless an approriate turbulence model is chosen with the correct empirical constants, turbulence model prediction may be less consistent than the laminar model for a BFB. This is also mentioned by Lundberg [8].

The restitution coefficient e is dependent on the bed material. Both [61] and Taghipour *et al.* [60] found that values between 0.9 and 1 gave similar results compared to the experimental results.

In regards to wall functions, Chanchal [61] concluded that simulations with free slip and no slip have approximately the same bubbling frequency, but the bubble shapes show better similarity with the experimental values when free slip is applied, however more emperical data is needed to properly determine the right wall function.

Perrone and Amelio [62] modelled the conductive and convective heat transfer in a BFB, comparing the heat transfer coefficient at different inlet gas temperatures, respectively 20 ^{o}C and 800 ^{o}C.

Krishnamoorthy *et al.* [63] modelled the multiphase hydrodynamics in a photo bioreactor comparing different multiphase models and proposed a methodology for modelling radiation in multiphase flows. As mentioned in this research, there is a lack of rigorous coupling between radiative transfer and hydrodynamics in simulations of non-dilute multiphase flows. This is due to to the high computational cost, complexities arising from the need to incorporate additional equations and terms within current RTE solution frameworks of (commercial) CFD codes, and incompatibilities in the output and input variables that are employed by the radiation and multiphase models. The goal was not validation, but providing initial results towards the demonstration of a modelling methodology to couple radiative transfer and other multiphase models in a CFD framework.

Table 3.1: Overview reference literature for modelling a BFB

Literature & Parameter Overview	
Hydrodynamics	
Authors	*Parameters*
Chanchal [61]	• Drag model – Syamlal-O Brien model – Gidaspow model – EMMS model – McKeen model • Wall boundary function – No slip – Partial slip • Restitution coefficient (0.85-1) • Viscous modelling – Laminar – Turbulent (k-ϵ model)
Lundberg [8]	• Drag model – Syamlal-O Brien model – Gidaspow model – RUC-drag model • 2D vs 3D modelling • Multiple particle phases (different sizes) • Discretization scheme (FOU, SOU)
Taghipour *et al.* [60]	• Drag model – Syamlal-O Brien model – Gidaspow model – Wen & Yu model • Inlet Velocity primary phase • Restitution coefficient (0.9-0.99) • Viscous modelling
Heat Transfer	
Krishnamoorthy *et al.* [63]	• Multiphase models – Two-Fluid model (TFM) – Mixture model – Dense Discrete Phase model (DDPM) – Two-Fluid model (TFM) with population balance • Inlet Velocity primary phase
Perrone and Amelio [62]	• Inlet Temperature

3.3.2. PARAMETER SELECTION

Parameters are investigated in order to make the model closer to the experimental findings. Experimental validation is however not possible at the moment of conducting this research and because of that, only certain parameters are selected to investigate. In regards to modelling the hydrodynamics of the IH-BFBSR, this research will focus on a drag model comparison between the Gidaspow and Syamlal-O Brien model and evaluate the hydrodynamic behaviour.

In regards to solving the heat transfer, this research will follow the proposed methodology mentioned by Krishnamoorthy *et al.* [63] for modelling the radiation. Furthermore the conductive heat transfer will be temperature dependent, being a continuation of the methodology proposed by Perrone and Amelio [62].

Varying parameters such as the inlet velocity and restitution coefficient to evaluate the hydrodynamics will not be discussed in this thesis and it is also assumed there is no slip for both phases regarding the wall boundary function.

Higher order discretization schemes give more accurate results. At the moment of conducting this research, no experimental data is available to validate the CFD results. Therefore, only a First Order Up (FOU) discretization scheme will be applied in the CFD modelling of the IH-BFBSR.

To reduce the computational time, 2D modelling is selected for this case and the results for 2D cases are generally deemed sufficient for predicting the hydrodynamics in a BFB.

4

MODEL IMPLEMENTATION IN ANSYS® FLUENT

4.1. CASE DESCRIPTION

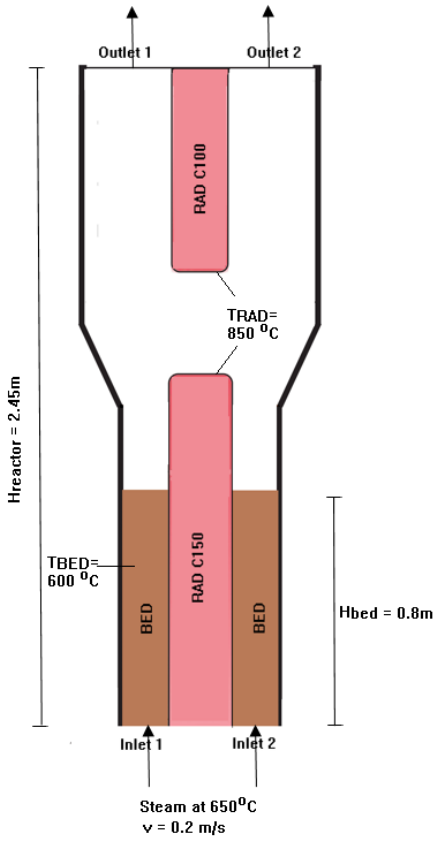

Figure 4.1: Schematic overview of the case description of the IH-BFBSR.

This problem considers the IH-BFBSR in which preheated steam at 650 ^{o}C flows upwards through the bottom of the domain through two inlets. The reactor is filled up with corundum particles to a height of 0.8 m, and the bed is assumed to be initially at rest with an initial voidage ϵ of 0.4. The bed particles are assumed to be spherical and of uniform size, with a diameter of 352 μm. Furthermore it is assumed the bed is already preheated, at a uniform temperature of 600 ^{o}C. The surface temperature of the radiant tubes is assumed to be constant at 850^{o}C. The operating inlet velocity is set to be 2.5 times the minimum fluidization velocity and the operating pressure is set to the ambient pressure. The steam leaves the reactor through two outlets, and in the operating bubbling fluidized bed regime, the bed particles are expected to stay within the reactor.

Material properties such as the density ρ, viscosity μ and the specific heat C_p of the steam and corundum, have been assumed to be temperature independent, and this will be further discussed in section 4.2.4. Table 4.1 gives an overview of the dimensions and preset conditions for the modelling of the IH-BFBSR.

Table 4.1: Preset Parameters

Properties	*Value*	*Notes*
Dimensions [m]		
Bed Height	0.800	
Inlet Diameter	0.103	
Outlet Diameter	0.176	
RAD C100 Diameter	0.100	
RAD C150 Diameter	0.145	
RAD C100 Length	0.750	
RAD C150 Length	1.150	
Reactor Length	2.453	
Operating Conditions		
Initial Bed Voidage ϵ	0.4	
Minimum Fluidization velocity U_{mf} [m/s]	0.08	equation 2.8
Inlet Velocity [m/s]	0.2	2.5 ·U$_{mf}$
Reynolds Number Re_{mf}	0.18	equation 2.8

4.2. MODEL IMPLEMENTATION

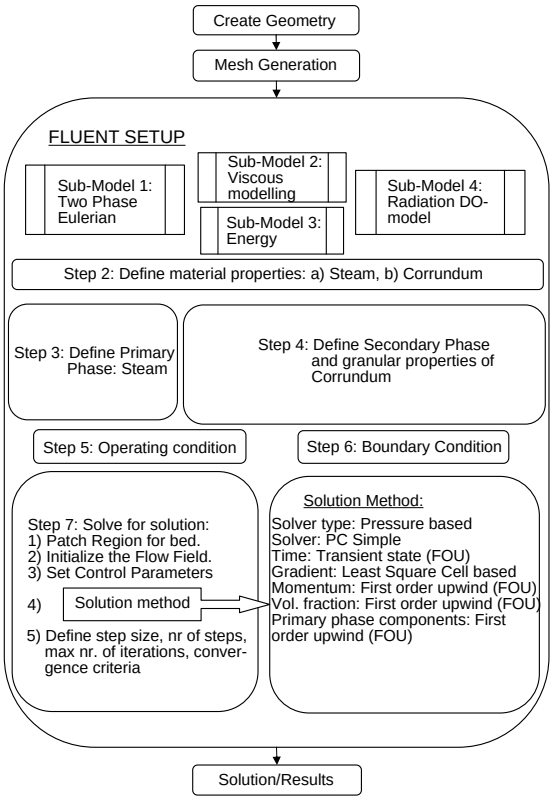

Figure 4.2: Flow diagram of the general procedure setting up a 2D BFB case.

Figure 4.2 gives an overview of the steps taking to set up the case file in ANSYS® FLUENT. Before the implementation in ANSYS® FLUENT, first the geometry and mesh must be created.

4.2.1. GEOMETRY AND MESH

The geometry was created in ANSYS® Design Modeler according to the dimensions shown in Table 4.1. The geometry was then imported into a "mesh generating" software, ANSYS® ICEM-CFD. Different types of mesh are available, a quadrilateral mesh, a triangular mesh or a hybrid mesh (containing both quadrilateral and triangular cells). Multiphase modeling is complex as the Eulerian multiphase model has a large number of coupled transport equations. In order to make the numerical solution converge, a fine grid is required to improve the accuracy, which will in turn increase the computational time. Both a hybrid mesh and quadrilateral mesh were considered. A quadrilateral mesh was chosen as it reduces the density of the mesh while keeping the number of nodes the same. This decreases the computational time substantially, compared to the hybrid mesh. Figure 4.3 shows the geometry and part of the mesh of the IH-BFBSR.

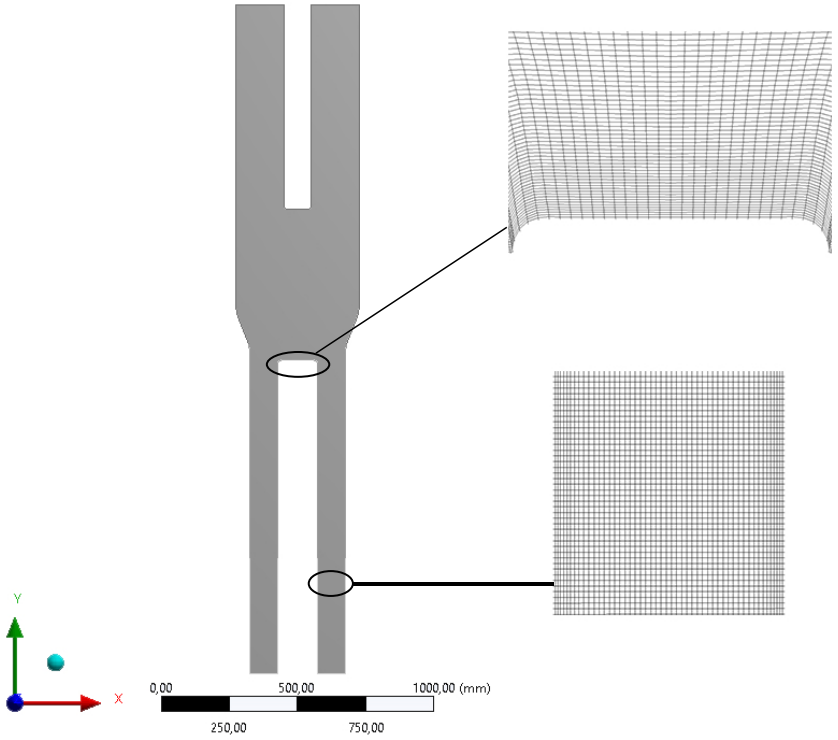

Figure 4.3: Geometry and mesh of the IH-BFBSR.

The next step is deciding on the cell size of the mesh. A general rule of thumb for modelling multiphase flows, is that the mesh cell size should be less than or equal to 10 times the particle diameter to get mesh independent results, as reported by Syamlal and O'Brien [64] and Zimmermann and Taghipour [65].

At the wall, the mesh cell size was refined to 1 x 2 mm to account for the expected high velocity and temperature gradients near the wall. In the bed region, the cell size increases towards the center to approximately 2 x 2 mm (≈ 6 times the bed particle size). For the freeboard section, the cell size is increased up to 5 x 9 mm towards the center, and at the outlet of the reactor up to 3 x 30 mm. The particles are expected to stay within the bed region under the chosen operating conditions, thus only a very fine mesh is required for the bed region, and the computational time is reduced.

Before being imported into ANSYS® FLUENT, the mesh must conform to the following to generally ensure good numerical results:

- a minimum quality of 0.3.
- a minimum angle of 18.
- smooth cell size change.

Figure 4.4 shows the number of cells versus the quality and angles, for the mesh of the IH-BFBSR which contains 81740 elements in total. The arrows indicate the number of cells with a certain quality or angle is much higher than the values shown in Figure 4.4.

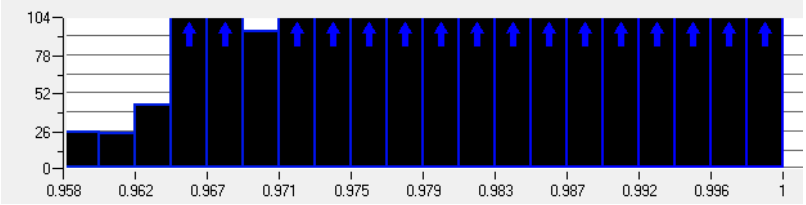

(a) Quality mesh.

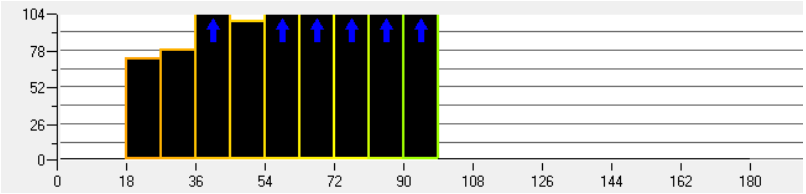

(b) Angle mesh.

Figure 4.4: Overview Quality and Angle of the mesh.

4.2.2. GENERAL SETTINGS

With the mesh imported into ANSYS® FLUENT, the simulation can be setup. A pressure based solver is chosen, and a transient simulation is selected. The gravity g is specified as 9.81 m/s^2.

The pressure-based solver employs an algorithm where the constraint of mass conservation (continuity) of the velocity field is achieved by solving a pressure (or pressure correction) equation. The pressure equation is derived from the continuity and the momentum equations in such a way that the velocity field, corrected by the pressure, satisfies the continuity. Since the governing equations are nonlinear and coupled to one another , the solution process involves iterations wherein the entire set of governing equations is solved repeatedly until the solution converges [11].

The domain is discretized into finite number of control volumes (CV), where for every CV, the governing equations for the solution variables are solved one after another sequentially or simultaneously. The computational node lies at the centre of the CV and an interpolation method is used to express variable values at the CV surface in terms of the nodal values.

4.2.3. MODEL SELECTION

The next step is to define the models (discussed in section 3.1 and 3.2). For the first case, where the hydrodynamics are evaluated, only the two-phase Eulerian model is selected, and when analyzing the heat transfer, the energy equation and radiation model are selected as well. The flow is considered laminar (for packed beds) when the Reynolds number is equal or less than 10, which is the case under the current operating conditions. In regards to radiation, strong forward scattering is assumed, and the constant C in the linear anisotropic phase function has been set to 1.

4.2.4. DETERMINING MATERIAL PROPERTIES

Having set up the models, the next step is to define the material properties. Properties such as the viscosity and density have a big influence on the hydrodynamic behaviour of the bed. When these properties are defined as temperature/pressure- dependent, a more accurate representation of the real time operation would be expected. However temperature dependent properties add to the complexity of modelling multiphase flows and may cause unwanted behaviour such as reverse flows at the outlet and/or divergence of the numerical solution.

As the modelling of the IH-BFBSR gets more complex by adding the energy and radiation equation while solving the continuity equations, the density ρ, viscosity μ and specific heat C_p have been chosen to be constant in the modelling with and without heat transfer.
Figure 4.5 shows the temperature dependence of the density and viscosity of steam, where the values have been taken from the NIST database. The temperature range chosen to derive the mean property values of steam is between 650 - 850 ^{o}C.

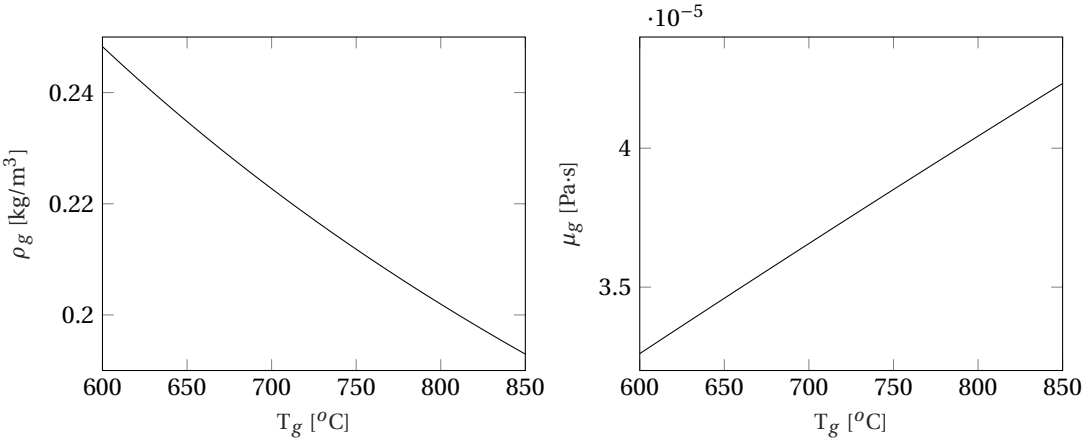

(a) Density of steam

(b) Viscosity of steam

Figure 4.5: Thermal dependence of properties Steam.

The density of corundum is set at 3950 kg/m^3, and the viscosity will be derived from the KTGF. Table 4.4 give an overview of the input values for the density and viscosity of steam and corundum.

Table 4.2: Input values for density,viscosity of steam and corundum

Property	*Model/ Value*	*Notes*
ρ_g [kg/m^3]	0.21	mean deviation: 6.3%
ρ_s [kg/m^3]	3950	
μ_g [Pa·s]	3.85 e-5	mean deviation: 6.5%
μ_s [Pa·s]	KTGF	equation 3.18

4.2.4.1. THERMAL PROPERTIES

For modeling the heat transfer, the thermal conductivity, specific heat, the scattering and absorption coefficient (in case the radiation model is implemented) of both steam and corundum must be defined. Figure 4.6a shows the temperature dependence of the specific heat of steam and corundum.

The effective thermal conductivity of the steam and gas is dependent on the microscopic thermal conductivity of each phase, and the volume fraction in each cell. Perrone and Amelio [62] assumed the microscopic thermal conductivity to be temperature independent, however in this case is assumed to be temperature dependent, as shown in Figure 4.6b .

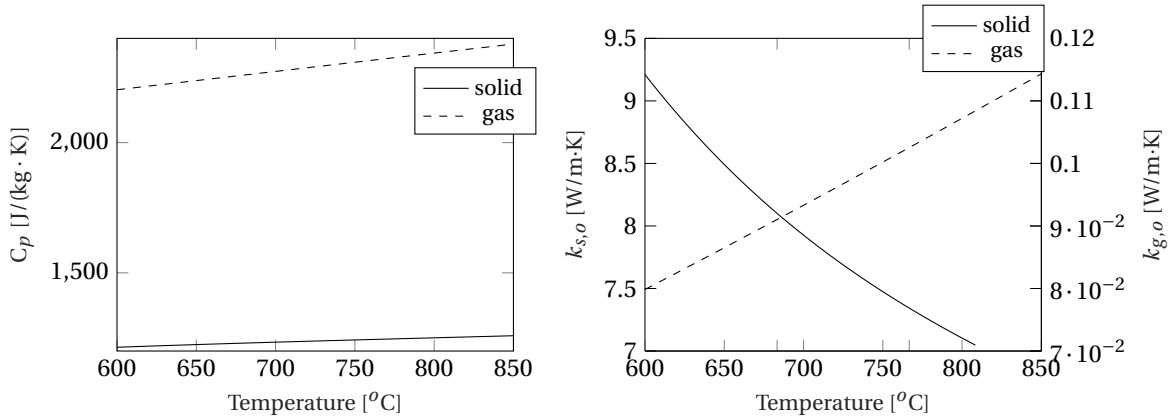

(a) Specific Heat C_p

(b) Microscopic Thermal conductivity k_o

Figure 4.6: Thermal dependence of properties steam and corundum.

Figure 4.7 shows the volume fraction dependence of the effective thermal conductivity of the steam k_g, corundum k_s and mixture/bed k_b at a temperature of 850 ^{o}C. It can be seen that the effective thermal conductivity of the bed k_b is significantly smaller than the microscopic thermal conductivity of corundum particles $k_{s,o}$ (seen in Figure 4.6b).

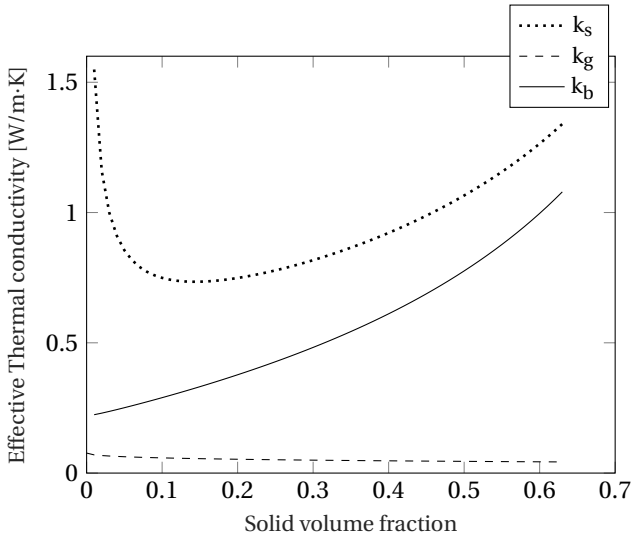

Figure 4.7: Volume fraction dependence of the effective thermal conductivity at T= 850 ^{o}C.

The radiation properties are dependent on the optical properties (n,k) and the size parameter x (equation 2.25a and 2.25b). The radiant tubes operate at 850 ^{o}C. According to Planck and Wiens displacement law (equation 2.15), the radiation intensity peaks at a wavelength of approximately 2.6 μm. Therefore, the radiation properties will be calculated for wavelengths between 0-10 μm. The optical properties are not only wavelength dependent but also temperature dependent, however no data was available for the optical properties of corundum at high temperatures. As a reference, the optical data is taken from measurements by Kischkat *et al.* [66] at ambient temperature. Figure 4.8 showcases the optical properties of corundum and the size parameter x, dependent on the wavelength λ.

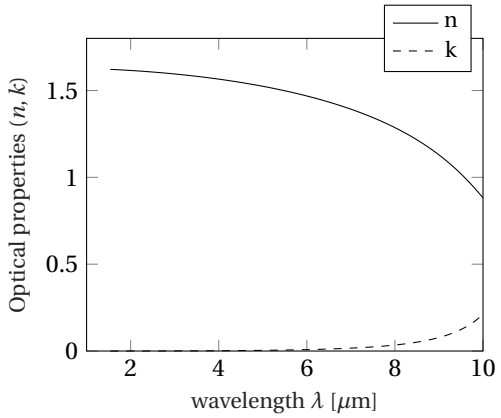

(a) Real (n) and imaginary (k) parts of refractive index.

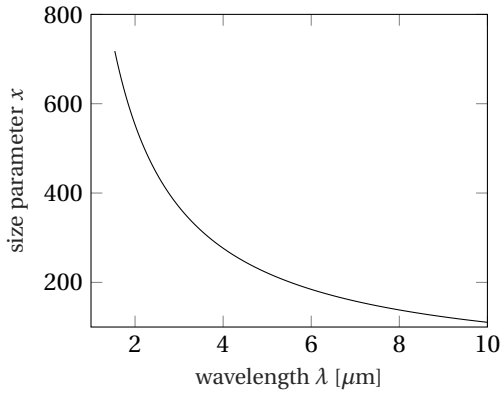

(b) Dimensionless size parameter x in wavelength interval.

Figure 4.8: Wavelength dependence of the optical properties of corundum.

As the size parameter $x > 1$ and $n \gg k$, corundum behaves like a dielectric for the chosen wavelength interval. A gray body model is assumed, thus the radiation properties are wavelength independent, and the mean hemispherical absorptivity α^s within the wavelength interval is calculated being 0.909, equal to the absorption efficiency Q_{abs}. Then the absorption and scattering coefficient can be derived. Figure 4.9 shows the absorption coefficient a_s and scattering coefficient σ_s of the bed as a function of the solid volume fraction α_s.

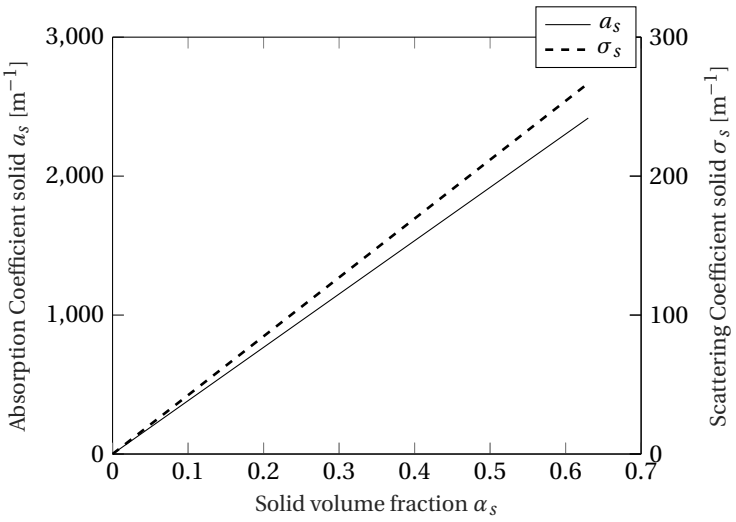

Figure 4.9: Volume fraction dependence of the absorption and scattering coefficient of the solids.

For the steam, the absorption coefficient has been taken from reference[50], where it is calculated as a function of temperature (valid up to temperatures of 2500 K) as:

$$\begin{aligned} a_s = -0.23093 - 1.12390\left(\frac{1000}{T_g}\right) + 9.41530\left(\frac{1000}{T_g}\right)^2 \\ -2.99880\left(\frac{1000}{T_g}\right)^3 + 0.51382\left(\frac{1000}{T_g}\right)^4 - 1.86840e^{-05}\left(\frac{1000}{T_g}\right)^5 \end{aligned} \tag{4.1}$$

It is assumed the bed will be dominant in the absorption and scattering of the radiation, and scattering is neglected for the steam. Table 4.3 gives an overview of the input values of the thermal properties of steam and corundum.

ANSYS® FLUENT did not incorporate volume-fraction and/or temperature dependent properties like the effective thermal conductivity, the absorption and scattering coefficient, so they must be implemented through user defined functions (UDF's).

Table 4.3: Thermal properties of steam and corundum particles.

Property	*Model/ Value*	*Notes*
$C_{p,g}$ [J/(kg · K)]	2290	mean deviation: 1.9%
$C_{p,s}$ [J/(kg · K)]	1238	mean deviation: 1.8%
k_g [W/m·K]	UDF	equation 3.29a
k_s [W/m·K]	UDF	equation 3.29b
a_g [m^{-1}]	UDF	equation 4.1
$\sigma_{s,g}$ [m^{-1}]	UDF	equation 2.27
$\sigma_{s,s}$ [m^{-1}]	UDF	equation 2.28
C	1	equation 3.32

4.2.5. IMPLEMENTING UDF

The UDF extracts the data of the volume fraction and temperature of every cell, which is then processed by the UDF giving an output value for the volume-fraction and/or temperature dependent properties, returning them back to each cell. The UDF's can be viewed in Appendix A. The basic principle is shown in Figure 4.6

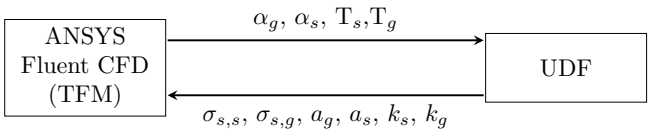

Figure 4.10: Flow diagram depicting the exchange of variables between the CFD calculations and the user-defined functions (UDFs).

4.2.6. DEFINING PHASES

Steam is defined as the primary phase (fluid/gas), while corundum is defined as a granular secondary phase (solids). Table 4.4 gives an overview of the granular properties of corundum.

Table 4.4: Granular properties of the secondary phase corundum.

Granular properties	*Value/Model*	*Notes*
Diameter [μm]	352	
Solid Pressure	*Lun-et-al*	equation 3.17
Radial distribution	*Lun et-al*	equation 3.16
Granular Viscosity	*Syamlal-obrien*	equation 3.20
Granular Bulk Viscosity	*Lun-et-al*	equation 3.22
Packing limit	0.63	Maximum solid volume fraction $\alpha_{s,max}$
Restitution Coefficient	0.9	

For the phase interaction, either the Gidaspow drag model or Syamlal-O'Brien drag model is selected. For the interphase heat transfer, the Gunn model is selected.

4.2.7. BOUNDARY CONDITIONS

At the inlet, the steam is set at a velocity of 0.2 m/s, with a temperature of 650 ^{o}C. The inlets are defined as a velocity inlet, and outlets are defined as a pressure outlet. A constant temperature of 850 ^{o}C is defined on the surface of the radiant tubes, while the wall on the outer-side of the reactor is assumed to be adiabatic (no heat flux). Furthermore the emissivity of the SiSiC radiant tube is assumed to be 0.9 [67].

4.2.8. SOLUTION METHOD

Before the solution is initialized, first suitable values for the time step size and under relaxation factors must be defined to make the numerical solution converge. The pressure-based solver uses under-relaxation of equations to control the update of computed variables at each iteration. The values of the under relaxation factors are usually determined through trail and error, until the solution converges. Table 4.5 gives an overview of the under relaxation values chosen for the modelling of the IH-BFBSR.

Table 4.5: Overview Under-Relaxation Factors.

Under-Relaxation Factors	*Value*
Pressure	0.2
Density	1
Body Forces	1
Momentum	0.1
Volume fraction	0.2
Granular Temperature	0.1
Energy	0.5
Discrete Ordinates	1

Generally a time step Δt of 0.001s is acceptable for multiphase modeling (used in this case), but Δt can also be determined by specifying a low Courant Nr. (preferably around 1), where the time step is defined as:

$$\Delta t = \frac{\text{Courant Nr.} \cdot \Delta x_{min}}{v}, \tag{4.2}$$

where Δx_{min} is the smallest cell dimension (in this case $\Delta x_{min} = 0.001$) and v is the inlet velocity (in this case $v = 0.2$ m/s).

The pressure based solver uses the The Phase Coupled SIMPLE (PC-SIMPLE) scheme (applicable for multiphase flows). The velocities are solved coupled by phases in a segregated fashion. Fluxes are reconstructed at the faces of the control volume and then a pressure correction equation is built based on total continuity. The coefficients of the pressure correction equations come from the coupled per phase momentum equations [11].

"First Order Upwind" discretization schemes were used in order to numerically solve the gradient, momentum, volume fraction and energy equation in each CV. At the end of each solver iteration, the residual sum for each of the conserved variables is computed and stored. The residuals are the measure of convergence of the iterative approach. The smaller the residual value, the more accurate the numerical solution is. For complex flows, if the residual of the continuity is 1e-3 or less, the solution is deemed acceptable. For the energy equation, a residual of 1e-6 or less is deemed acceptable. The number of iterations was set to 60, in order for the continuity residual to reach a value below 1e-3 during each time step. For the post-analysis, data was sampled at every 0.1s.

4.2.9. POST PROCESSING

After the simulation has ended, the results are post-processed in ANSYS® CFD-Post in order to obtain contour plots and also post-processed in MATLAB®, in order to calculate time-averaged properties of interest, to evaluate the hydrodynamics and heat transfer. Equation 4.4 shows how the time-averaged properties $\langle f(t) \rangle$ are calculated:

$$\langle f(t) \rangle = \frac{1}{t_2 - t_1} \sum_{t_1}^{t_2} f(t) \cdot \Delta t, \tag{4.3}$$

where Δt is equal to 0.1s.
For the heat transfer analysis, thermal properties of the mixture will be evaluated (such as the effective thermal conductivity k_m), calculated through volume fraction averaging given as:

$$f_m = \alpha_s f_s + \alpha_g f_g, \tag{4.4}$$

where f_s and f_g are properties of the solids and gas respectively.

5

RESULTS AND DISCUSSION

5.1. HYDRODYNAMIC RESULTS

The first case will evaluate how the Gidaspow and Syamlal-O' Brien drag model influence the hydrodynamics within the IH-BFBSR. Figure 5.1 and Figure 5.2 showcases the solid volume fraction at different time steps throughout the simulation with a superficial steam inlet velocity of 0.2 m/s with the Gidaspow drag and Syamlal-O' Brien drag model respectively.

In both cases, with the inlet gas velocity exceeding the minimum fluidization velocity, spontaneous formation of tiny bubbles start at the inlet position which will rise through the fluidized bed. The bubbles grow in size due to the entrained gas and bubble coalescence. In this case, the bed is deep and has a small cross sectional area similar to Figure 2.5, thus the bubbles grow in size almost to the width of the bed which will cause slugging. Due to the increase in bubble diameter, the bubbles rise faster, and the bed gets expanded. As the bubbles reach the top of the bed, the bubbles collapse, ejecting the particles. The particles do not reach the freeboard section, under the specified operating conditions.

With the geometry and mesh being symmetric around the y-axis and the boundary conditions being the same at both inlets and outlets, a symmetric hydrodynamic behaviour was expected in both beds beside the radiant tube. This holds true for the single phase modelling which can be viewed in Appendix B. For the multiphase simulation, this is not the case and the bubble formation and coalescence become more independent in each section as time goes on. It was looked into whether a smaller mesh size would resolve the asymmetric behaviour, but this did not seem to be the case. Another plausible cause could be the numerical solver, however this has not been further looked into. The bed on the right hand side (RHS) of the radiant tube will be used as a reference for the comparisons between the drag models and for the heat transfer simulation.

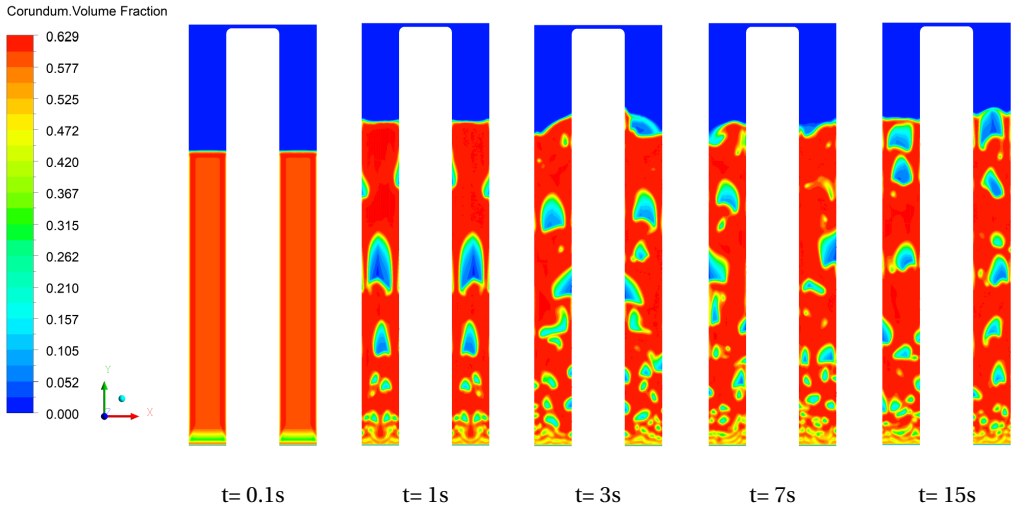

Figure 5.1: Solid volume fraction at different time steps with Gidaspow drag model

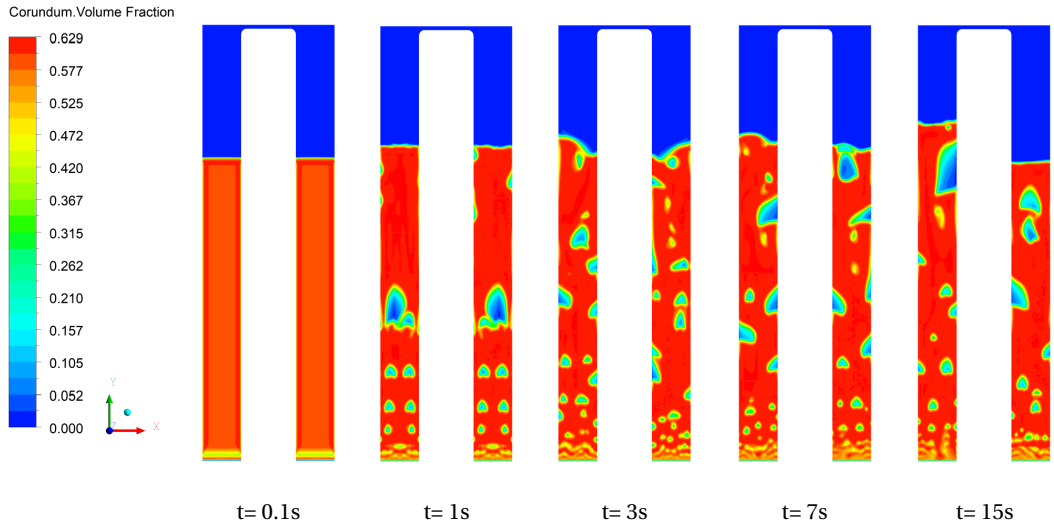

Figure 5.2: Solid volume fraction at different time steps with Syamlal-O' Brien drag model

With regard to the bubbling behaviour, the Gidaspow drag model predicts more bubbles forming at the inlet of the reactor, and growing bigger in size, compared to the Syamlal-O' Brien model. In the Syamlal-O' Brien model, more bubbles form at the outer wall of the reactor, the bubbles do not grow as fast in size, and bubble coalecence is less frequent.

Due to the Gidaspow model predicting bigger bubbles, the bed expansion of the Gidaspow model is slightly higher than when the Syamlal-O' Brien model is applied. For the evaluation of the hydrodynamics, the pressure P, axial velocity of the solids $v_{y,s}$, granular temperature Θ and solid volume fraction α_s were looked at. Figure 5.3a showcases the change in volume fraction through time according to the Gidaspow model and Figure 5.3a showcases the change in volume fraction according to the Syamlal-O-Brien model, both measured at a height of y = 0.4 m.

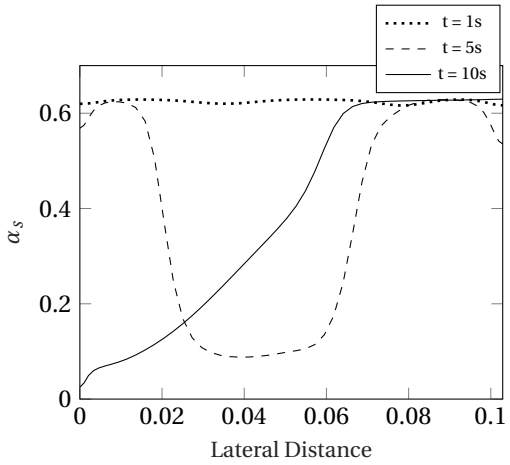

(a) Solid volume fraction according to the Gidaspow model.

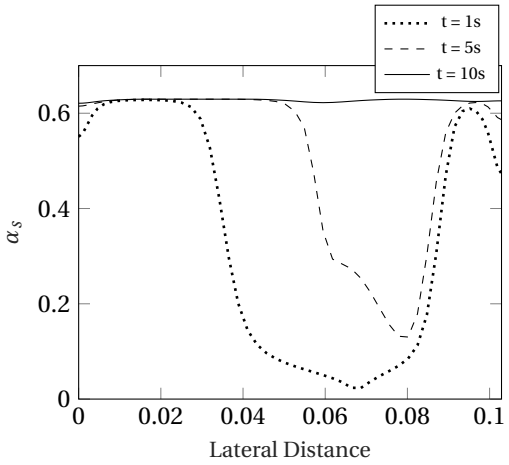

(b) Solid volume fraction according to the Syamlal-O-Brien model.

Figure 5.3: Instantaneous solid volume fraction through time.

From Figure 5.3, it can be observed that the predicted instantaneous volume fraction according to the drag models is quite different at each time. In order to better understand the influence the drag models have on the hydrodynamics, the time-averaged properties have been calculated and evaluated.

Figure 5.4 shows the time-averaged volume fraction $\langle \alpha_s \rangle$ as a function of the length of the reactor and the lateral distance across the inlet. Data was sampled at every 0.1 second and is averaged over 20 seconds.

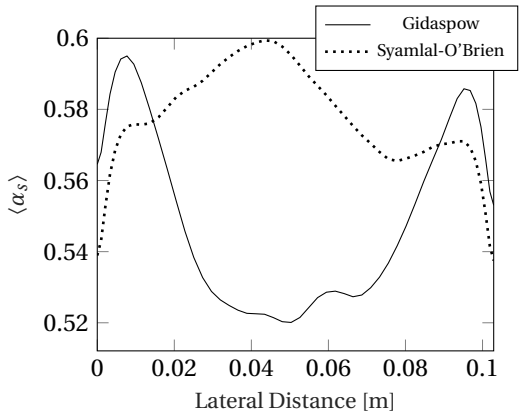

(a) Time averaged solid volume fraction distribution in the lateral direction calculated at h= 0.4 m.

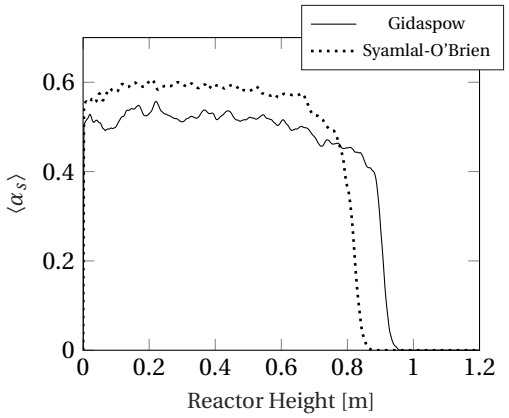

(b) Time averaged solid volume fraction distribution along the central axis of inlet 2.

Figure 5.4: Solid Volume Fraction Drag model comparison.

As seen in Figure 5.4a, the Gidaspow model predicts a higher solid volume fraction near the walls of the reactor than the Syamlal-O'Brien model. This is caused by the Syamlal-O'Brien model predicting a higher formation of bubbles near the wall, thus the particles are pushed towards the center. The Gidaspow drag model predicts more bubbles flowing trough the central region of the bed, and the particles are pushed to the side of the reactor. The bed expansion can be derived from Figure 5.4b, where the Gidaspow model predicts an expansion up to approximately 0.94 m and the Syamlal-O'Brien model an expansion up to approximately 0.87m (measured where the solid volume fraction becomes less than 0.01).

In regard to the axial velocity $v_{y,s}$, the nature is the opposite to the volume fraction distribution. As seen in Figure 5.4, the Gidaspow model predicts a core annular structure of flow, with an upward velocity in the central region, and the particles moving downwards near the wall. The Syamlal-O'Brien model predicts an upward velocity near the walls, and the particles moving downward in the central region as seen in Figure 5.5.

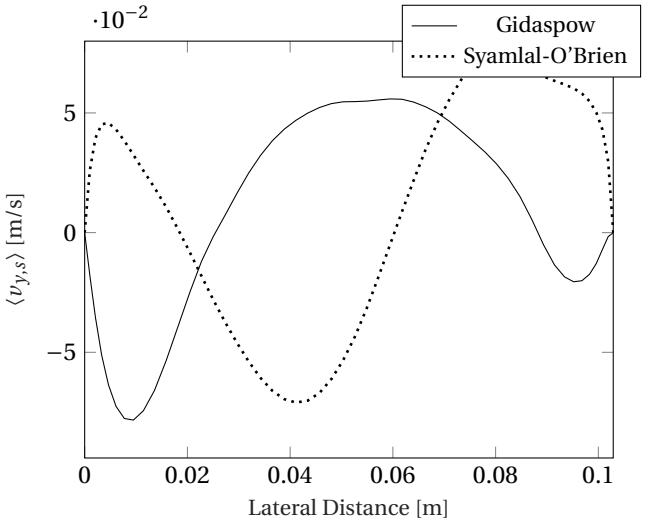

Figure 5.5: Time-averaged axial velocity distribution in the lateral direction at h= 0.4 m.

In regard to the granular temperature Θ, both the Gidaspow and the Syamlal-O'Brien model predict similar high granular temperatures near the wall compared to the central region, which is physically realistic according to Chanchal [61]. In the central region the granular temperature is slightly higher according to the Gidaspow model compared to the Syamlal-O'Brien model as seen in Figure 5.6.

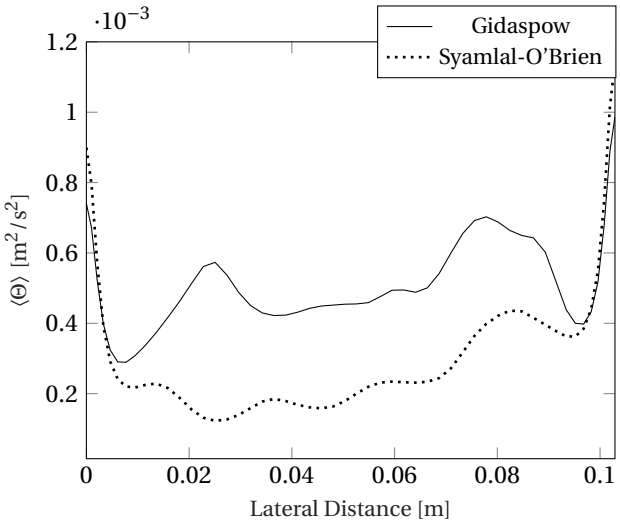

Figure 5.6: Time-averaged granular temperature distribution in the lateral direction at h= 0.4 m.

Next the pressure P will be evaluated (the pressure is the same for both phases), measured along the length of the reactor, at the center of inlet 2. The Gidaspow model predicts a slightly higher pressure drop of approximately 0.185 bar, and the Syamlal-O'Brien model predicts a pressure drop of approximately 0.18 bar (1 bar = $1 \cdot 10^5$ Pa).

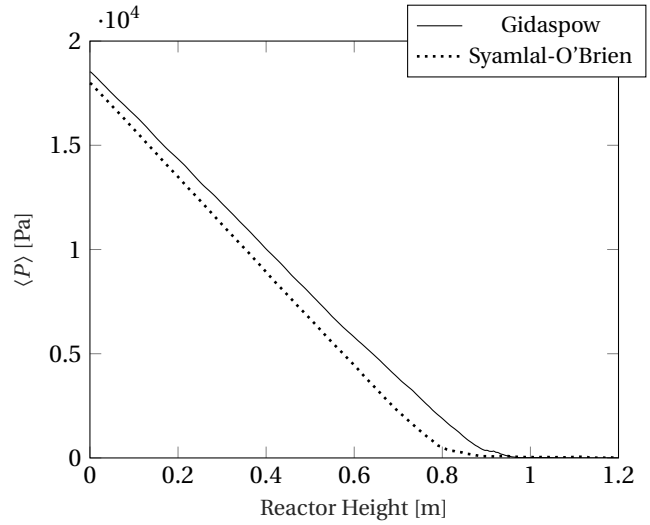

Figure 5.7: Pressure variation vs bed height.

Lastly the pressure as a function of time, at the initial bed height y = 0.8 m, will be evaluated and can be seen in Figure 5.8a. The pressure was first averaged over the width of the bed, before calculating the instantaneous pressure at the height of y = 0.8 m.

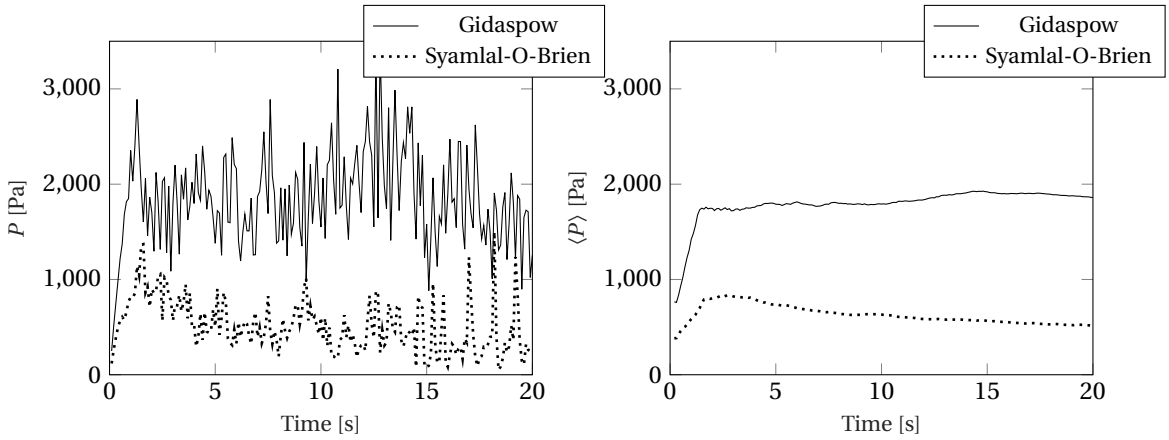

(a) Pressure variation as a function of time at y = 0.8 m.

(b) Time-averaged Pressure as a function of time at y = 0.8m.

Strong pressure fluctuations can be observed in Figure 5.8a. The pressure initially rises up to approximately 0.025 bar according to the Gidaspow model, and 0.013 bar according to the Syamlal-O-Brien model, both around t = 2 s. These strong fluctuations are caused by slugging, discussed in subsection 2.2.1.3. Figure 5.8b shows that the time-averaged pressure $\langle P \rangle$ according to the Gidaspow model reaches a steady state value around 0.018 bar and 0.006 bar according to the Syamlal-O-Brien model. Also it can be observed that both the Gidaspow and Syamlal-O-Brien model predict the bed gets fluidized around $t = 1.5$ s.

According to Chanchal [61], the Gidaspow drag model gives better predictions for the axial velocity profile (e.g. a core annular flow which is generally expected in fluidized beds) and solid volume fraction profile, while the Syamlal-O'Brien model gives better predictions for the granular temperature. As for the heat transfer evaluation, the Gidaspow model will be implemented because the thermal properties are dependent on the solid volume fraction.

5.2. HEAT TRANSFER RESULTS

For the heat transfer evaluation, first a simulation was run with only conductive transport and convective transport and the second simulation included radiation. Both simulations are discussed separately, and the contribution radiation has on the heat transfer behaviour within the IH-BFBSR is also looked at.

5.2.1. CONDUCTIVE AND CONVECTIVE HEAT TRANSFER

As mentioned in section 2.3, the first layer of particles, closest to the radiant tube wall, is the most important layer for heat transfer. The heat transfer from the radiant tube C150, the temperature profile within the reactor and the wall-to-bed heat transfer coefficient will be evaluated. Figure 5.9 shows the contour plot of the temperature profiles within the reactor at different times. The mixture temperature is evaluated, calculated through volume fraction averaging of the steam and corundum temperature.

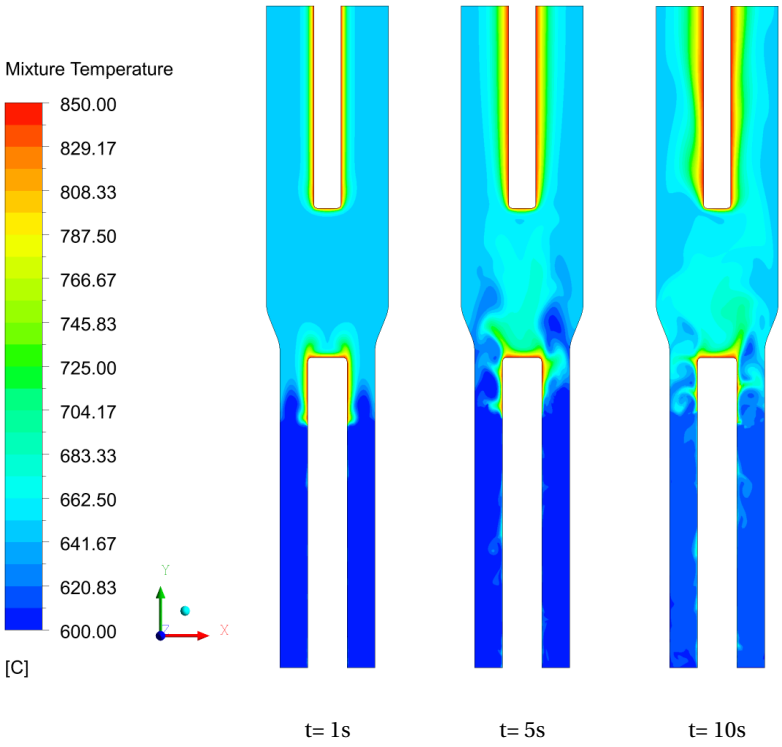

Figure 5.9: Temperature contour plot of the bed/mixture at different times.

The surface temperature of the bottom radiant tube C150 is fixed at 850 ^{o}C. The driving force of the heat transfer, is the temperature difference between the radiant tube and the bed/mixture temperature. With the bed initially at 600 ^{o}C and the steam at the inlet at 650 ^{o}C, the radiant tube will heat up both the steam and corundum particles. ANSYS® FLUENT predicts that the steam and corundum particles reach thermal equilibrium between each other very early on in the simulation. From Figure 5.9, it can be observed that after 10 seconds the temperature in the bed zone is mostly uniform and has slightly risen. This is due to the particle renewal near the radiant tube wall resulting in proper mixing.

The upper radiant tube C100, heats up the outgoing steam, and a temperature gradient can be observed ranging from 850 ^{o}C near the radiant tube wall, to 650 ^{o}C near the outer wall of the reactor. The heat transfer is further evaluated for the bed zone.

Figure 5.10 showcases the change of the temperature T in time as a function of the width of the bed, calculated at two different heights.

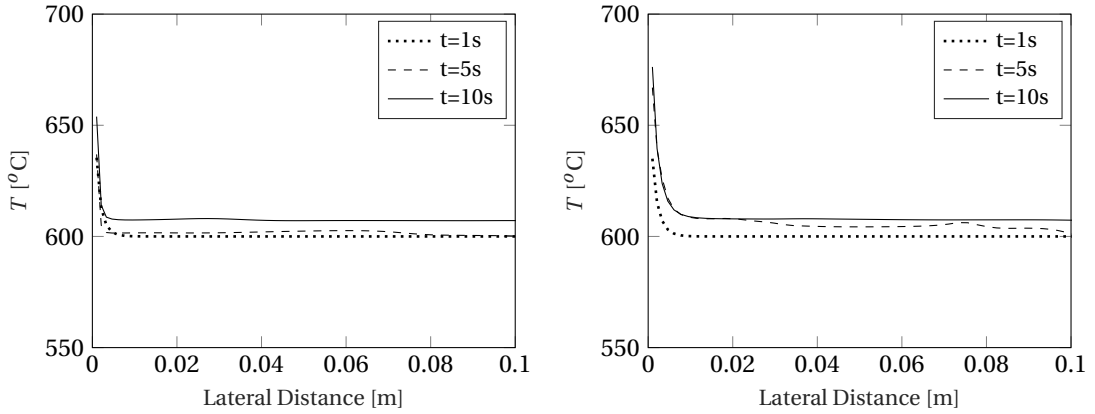

(a) Change of temperature profile in time measured at y= 0.4m.

(b) Change of temperature profile in time measured at y= 0.8m.

Figure 5.10: Temperature Profile over the width of the bed

The temperatures calculated near the wall at t = 1 s, are about the same at both heights, being approximately 635 ^{o}C near the radiant tube wall, and around 600 ^{o}C towards the outer wall of the reactor. After 10 seconds, near the radiant tube wall, a temperature rise of 18 ^{o}C can be observed at a height of 0.4 m and 41 ^{o}C at a height of 0.8 m. The mean temperature difference over the width of the bed (between t = 1-10 s) is approximately 7.3 ^{o}C at a height of 0.4 m and approximately 9 ^{o}C at a height of 0.8 m.

The first layer of particles close to the wall plays an important role in the heat transfer towards the bed and is evaluated next. The heat transfer is dependent on the temperature difference between the radiant tube wall and bed, and the effective thermal conductivity of the bed. Figure 5.11a showcases the temperature T, Figure 5.11b showcases the surface heat flux Φ_q emanating from the radiant tube C150, Figure 5.11c the effective thermal conductivity of the bed k_b and Figure 5.11d the solid volume fraction α_s, all as a function of the length of the radiant tube C150, calculated 1 mm away from the radiant tube at t = 10 s.

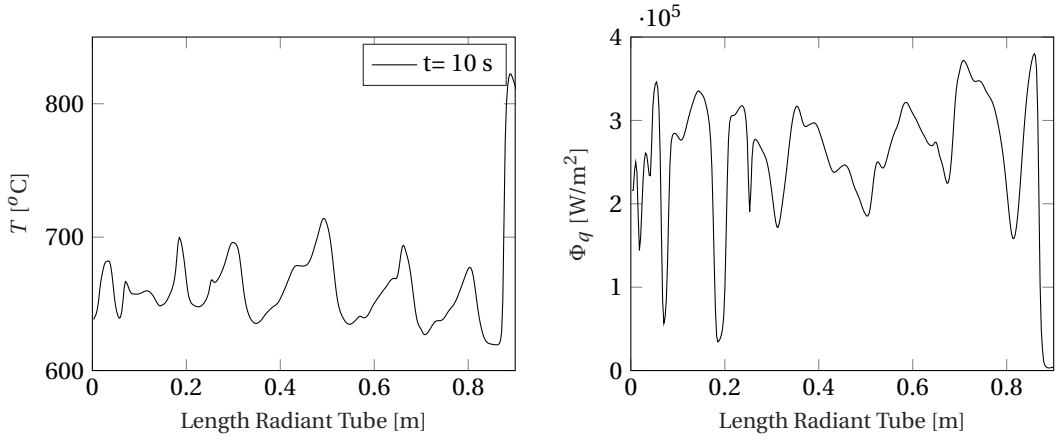

(a) Temperature profile over the length of the radiant tube.

(b) Surface Heat Flux from the radiant tube C150 over the length of the radiant tube.

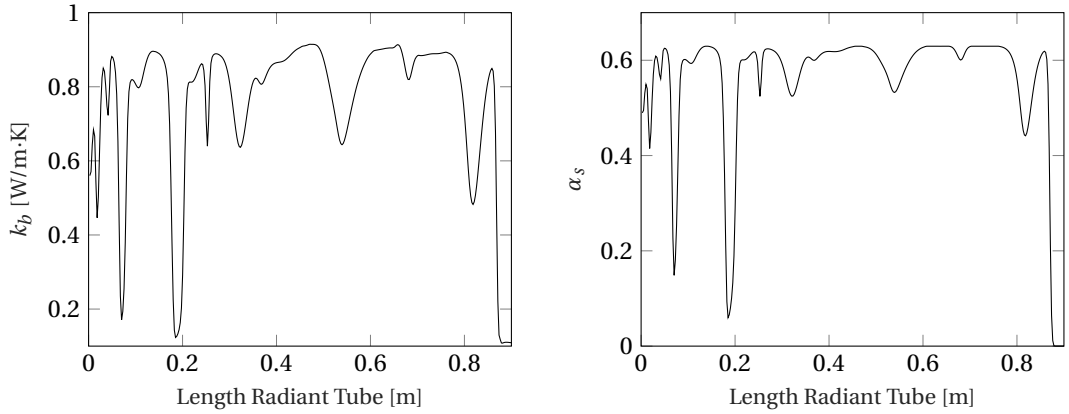

(c) Effective thermal conductivity over the length of the radiant tube.

(d) Solid Volume Fraction over the length of the radiant tube.

Figure 5.11: Heat transfer evaluation near the radiant tube wall.

As mentioned before, the main driving force behind the heat transfer is the difference in temperature between the radiant tube wall and the bed. From Figure 5.11 it can be observed the temperature T, surface heat flux Φ_q, effective thermal conductivity k_b and solid volume fraction α_s all exhibit oscillatory behaviour. This is due to the bubbles rising throughout the bed, entering and leaving the cells. Where the bed temperature peaks in Figure 5.11a, the surface heat flux will be at its minimum in Figure 5.11b (due to the decrease in temperature difference), and vice versa. Furthermore the surface heat transfer flux is also dependent on the effective thermal conductivity of the bed, which is a solid volume fraction dependent property. Where the solid volume fraction peaks, so does the surface heat flux and thermal conductivity and vice versa. When the solid volume fraction is low (e.g. when there are bubbles near the wall), the effective thermal conductivity drops due to the steam having a lower conductivity than the corundum particles as shown in Figure 4.7. The relation between the temperature and the solid volume fraction can be derived; where the solid volume fraction near the radiant tube wall is at a minimum (e.g. bubbles near the wall), the calculated bed temperature peaks, and vice versa.

The behaviour near the wall is summarized in Table 5.2, showcasing the correlation coefficient of the solid volume fraction, total surface heat flux, effective thermal conductivity and temperature, using the solid volume fraction as the reference data.

Table 5.1: Overview Correlation Coefficient of α_s.

Property	*Correlation Coefficient*
α_s	1
Φ_q	0.96
k_b	0.99
T	-0.91

Values close to 1 indicate that there is a positive linear relationship between the property and the solid volume fraction, values close to -1 indicate that the property has a negative linear relationship to the solid volume fraction, and values close to or equal to 0 suggest there is no linear relationship between the property and the solid volume fraction.

Lastly the wall-to-bed heat transfer coefficient h will be calculated. This is done by dividing the surface heat flux by the temperature difference between the radiant tube and the bed distanced 1 mm away from the radiant tube wall. Figure 5.12 showcases the instantaneous wall-to-bed heat transfer coefficient h as a function of the length of the radiant tube, at t = 10 s.

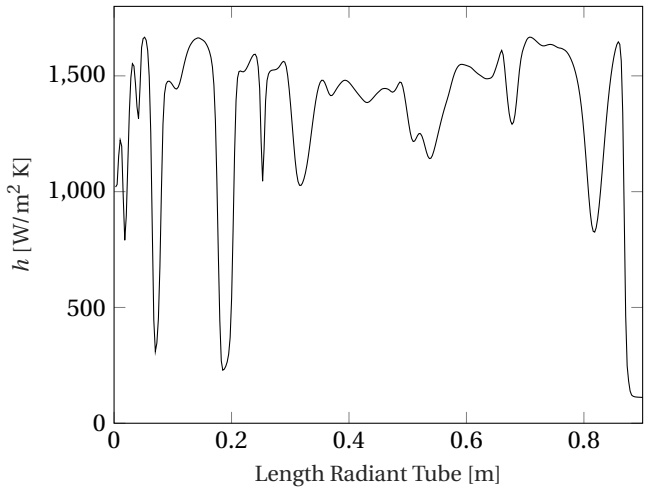

Figure 5.12: Instantaneous wall-to-bed heat transfer coefficient as a function of length of the reactor.

Again a similar oscillatory pattern can be observed for the instantaneous heat transfer coefficient h. The heat transfer coefficient peaks where the solid volume fraction is high, thus the thermal conductivity is high, and vice versa.

Figure 5.13 showcases the time-averaged wall-to-bed heat transfer coefficient $\langle h \rangle$ as a function of time. Prior to time averaging, the wall-to-bed heat transfer coefficient was averaged along the length of the radiant tube up to 0.9 m (the expected bed expansion height) at each time step. Data was sampled at every 0.1 second and is averaged over 10 seconds.

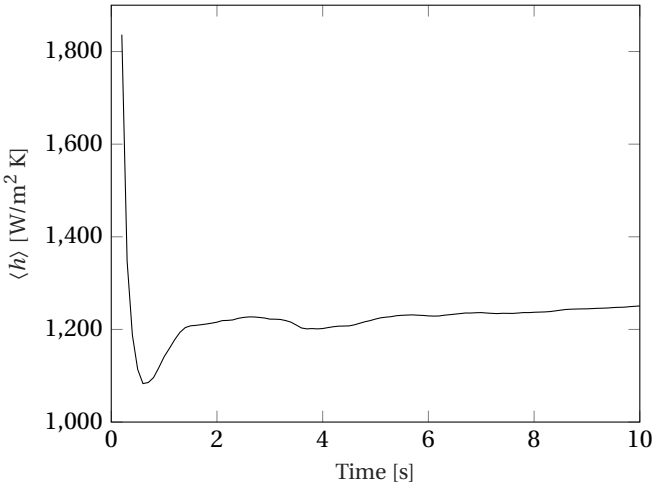

Figure 5.13: Time-averaged wall-to-bed heat transfer coefficient as a function of time.

The time-averaged wall-to-bed heat transfer coefficient shows a sharp decrease in the first two seconds (due to the initial high temperature difference), and reaches more or less a steady state value around 1228 W/ (m^2 K). The behaviour of $\langle h \rangle$ is similar to the numerical results of Kuipers *et al.* [26], who compared their numerical results to the penetration theory. Next the heat transfer including radiation is evaluated.

5.2.2. HEAT TRANSFER INCLUDING RADIATION

The heat transfer including radiation is analyzed and discussed in a similar fashion to section 5.2.1. Figure 5.14 showcases the contour plot of the temperature profile within the reactor at different times.

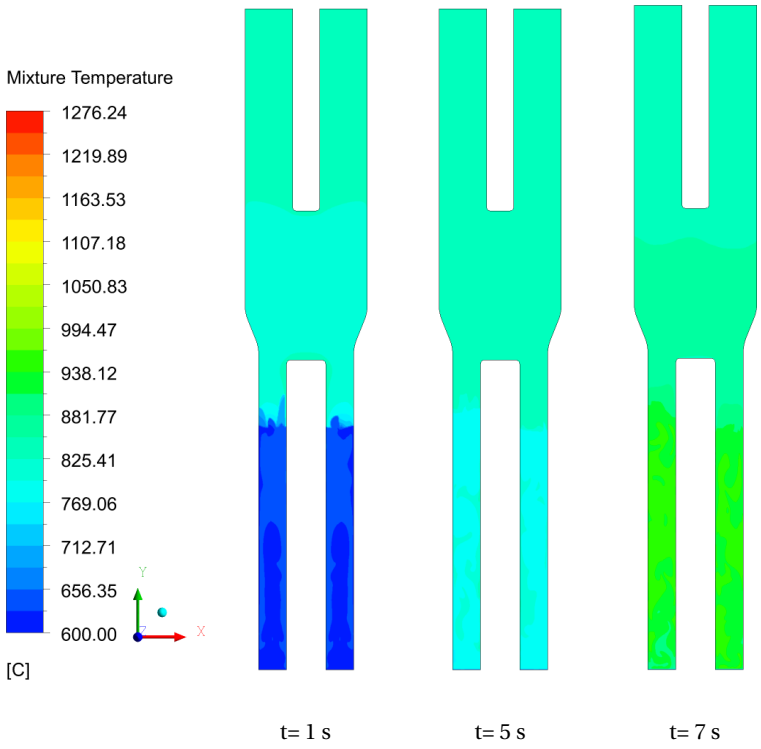

Figure 5.14: Temperature contour plot of the bed/mixture at different times, including radiation.

As can be seen from Figure 5.14, there is are some cold spots at t = 1 s, occurring where the bubbles are within the reactor, the central region and near the walls, in this case. This could be due to to the bed particles being dominant in the absorption of the radiative heat flux. After 5 seconds, the temperature in the bed zone seems mostly uniform around 812 ^{o}C, and the temperature in the freeboard zone is around 850 ^{o}C. After 7 seconds, the bed temperature exceeds the radiant tube temperature. This is unwanted behaviour, as ideally the operating temperature throughout the reactor is supposed to be maintained around 850 ^{o}C. With the temperature being fixed over the radiant tube at 850 ^{o}C, and the outer wall of the reactor being adiabatic (zero heat flux), the bed absorbs most of the radiation. Running the simulation longer, results in the bed heating up continuously to even higher temperatures. Based on this behaviour, one could conclude that the current modified RTE might not be suitable to model radiation heat transfer for fluidized beds under current assumptions and input values. Nevertheless, these results could provide future insight into radiation modelling for multiphase flows, and comparing with experimental results can provide better comprehension on how the RTE and its parameters can be modified.

Figure 5.15 showcases the change of the temperature T in time as a function of the width of the bed, calculated at two different heights.

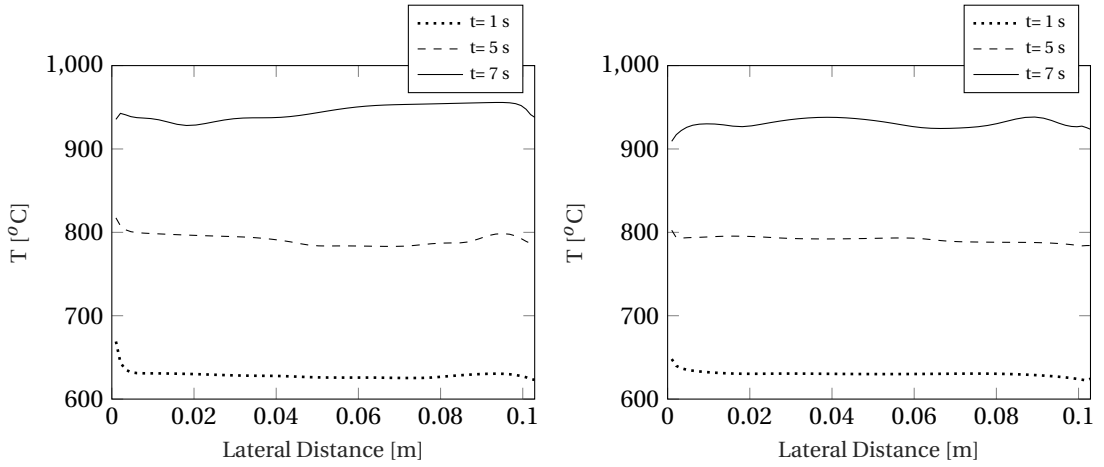

(a) Change of temperature profile in time measured at y= 0.4 m.

(b) Change of temperature profile in time measured at y= 0.8 m.

Figure 5.15: Temperature Profile over the width of the bed with radiation included

It can be seen at each time step, that the temperature is around the same magnitude over the width of the bed and no strong temperature gradient near the wall is observed like the case without radiation. This could be due to the strong forward scattering and the bed being optically thick, meaning that most of the radiation will be absorbed by the first layers of particles near the radiant tube wall. Furthermore the particles will also emit radiation resulting in the bed heating up faster, thus the temperature difference between the bed and wall becomes smaller. The mean temperature difference over the width of the bed (between t = 1-7 s) is approximately 315 ^{o}C at a height of 0.4 m and approximately 300 ^{o}C at a height of 0.8 m.

Next the first layer of particles close to the radiant tube C150 is evaluated at t = 5 s, where the bed temperature does not exceed the radiant tube temperature yet. Figure 5.16a showcases the temperature T, Figure 5.16b showcases the total surface heat flux Φ_q including the radiative heat flux emanating from the radiant tube C150, Figure 5.16c the absorption coefficient of the bed a_b and Figure 5.11d the solid volume fraction α_s, all as a function of the length of the radiant tube C150, calculated 1 mm away from the radiant tube at t = 5 s.

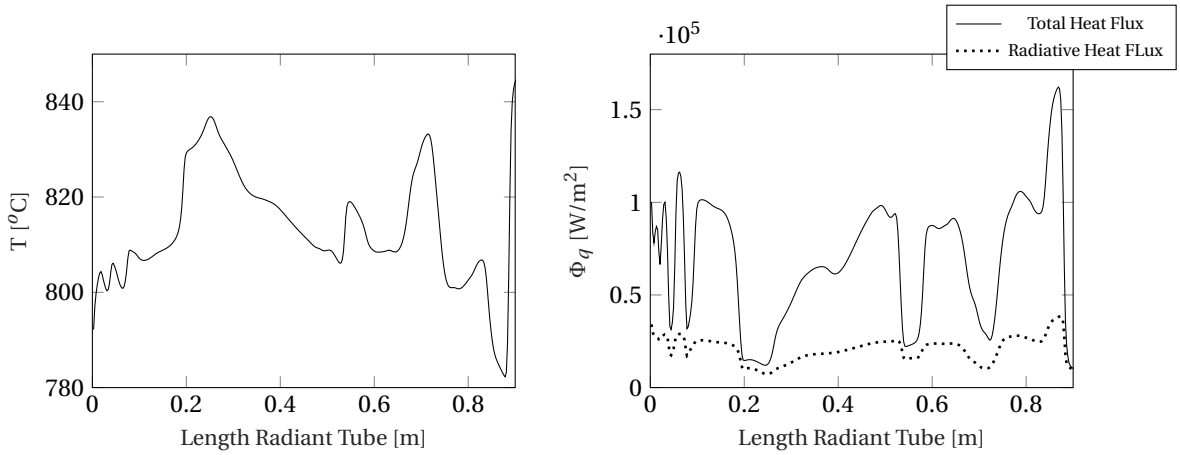

(a) Temperature profile over the length of the radiant tube.

(b) Surface Heat Flux from the radiant tube C150 over the length of the radiant tube.

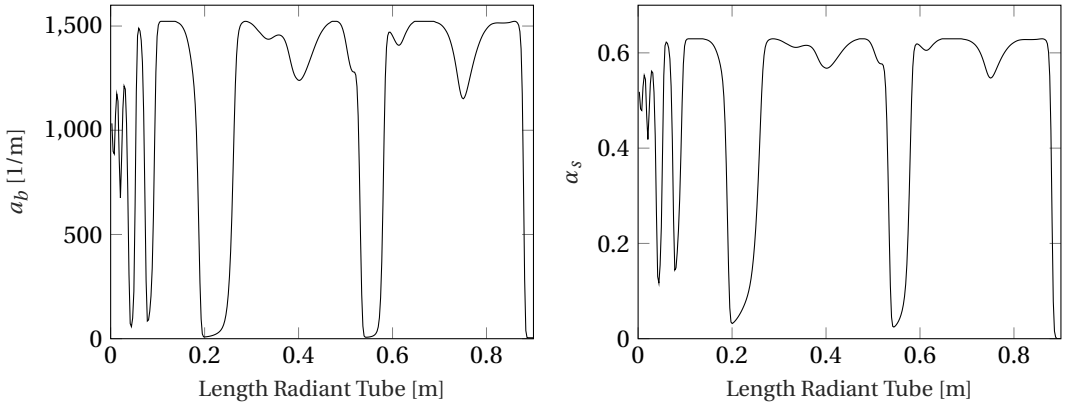

(c) Absorption Coefficient of the bed over the length of the radiant tube.

(d) Solid Volume Fraction over the length of the radiant tube.

Figure 5.16: Heat transfer evaluation near the radiant tube wall with radiation included.

Again oscillatory behaviour can be observed in Figure 5.16 for the temperature T, surface heat flux Φ_q, absorption coefficient of the bed a_b and solid volume fraction α_s. Where the solid volume fraction peaks, so does the total surface heat flux and absorption coefficient and vice versa. The surface heat flux is much smaller than the case without radiation, due to the driving force e.g. the temperature difference between wall and bed also being much smaller. The calculated temperature is inversely related to the solid volume fraction, where the solid volume fraction is low, the temperature peaks and vice versa. The particles will also emit radiation, and heat up each other. In ANSYS® FLUENT, there is no direct means to report how much radiation has been absorbed/emitted/scattered in each cell. However the total incident radiation, passing through the cell (in all directions) can be retrieved and is shown in Figure 5.17 as a function of the length of the radiant tube C150.

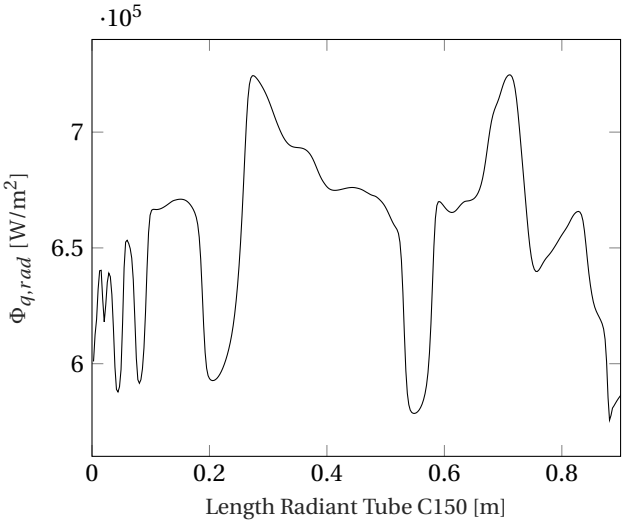

Figure 5.17: Incoming Radiative Heat Flux.

As can be seen, the total incident radiation is several times higher than the total surface heat flux emanating from the radiant tube (shown in Figure 5.16b). This is the reason the bed heats up fast, due to the current RTE (equation 3.30) over predicting the radiation that is emanating and scattered from the bed particles.

The behaviour near the wall is summarized in Table 5.2, showcasing the correlation coefficient of the solid volume fraction α_s , total surface heat flux Φ_q , absorption coefficient a_b , temperature T, and incident radiation $\Phi_{q,rad}$, using the solid volume fraction as the reference data.

Table 5.2: Overview Correlation Coefficient with radiation included.

Property	*Correlation Coefficient*
α_s	1
Φ_q	0.83
a_b	0.99
T	-0.73
$\Phi_{q,rad}$	0.86

Lastly the wall-to-bed heat transfer coefficient will be determined in the same way as the case without radiation. This will not be entirely accurate, as it is unknown how much of the radiative heat flux will be absorbed by the particles. Figure 5.18a showcases the instantaneous length-averaged heat transfer coefficient h along the length of the radiant tube and Figure 5.18b the time-averaged heat transfer coefficient $\langle h \rangle$ as a function of time.

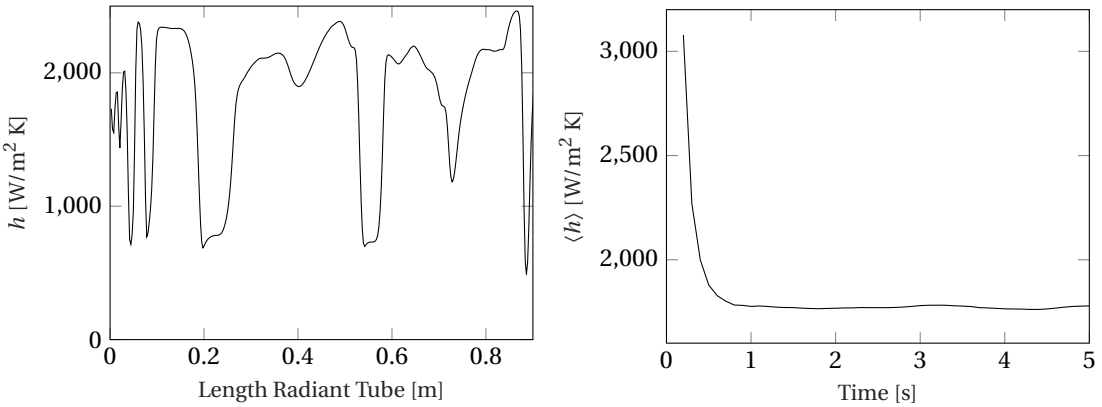

(a) Instantaneous wall-to-bed heat transfer coefficient as a function of length of the radiant tube.

(b) Time-averaged wall-to-bed heat transfer coefficient as a function of time.

Figure 5.18: Wall-to-bed heat transfer coefficient evaluation with radiation included

The instantaneous local heat transfer coefficient h has a positive correlation with the solid volume fraction behaviour. The time-averaged wall-to-bed heat transfer coefficient $\langle h \rangle$ shows a similar behaviour to the case without radiation, reaching a steady state value around 1771 W/ (m^2 K) after 1 second (which is 543 W/ (m^2 K) higher, than the case without radiation).

6

CONCLUSIONS AND RECOMMENDATIONS

This chapter presents the conclusions drawn from the hydrodynamic and heat transfer analysis within the IH-BFBSR and discusses how this research can be expanded and improved.

6.1. CONCLUSIONS

First a study was done on the physical phenomena occurring in a BFB, and what models were developed to describe the physical phenomena. The hydrodynamics were evaluated, and then the heat transfer, where the conductive and convective heat transport was looked at first, before radiation was added.

In regards to hydrodynamics, both the Euler-Euler and Euler-Lagrange approach seemed suitable to model bubbling fluidized beds and the Euler-Euler approach is applied as it is less computationally expensive than the Euler-Lagrange approach. The hydrodynamics are solved by the momentum conservation equation based on the Navier-Stokes equation. The motion of the particles is described by the kinetic theory of granular flow.

Next the parameters were identified that influence the hydrodynamics and the inter-phase drag coefficient was chosen to investigate. Two drag models were evaluated, the Gidaspow drag model and the Syamlal-O-Brien drag model. Based on past literature, the Gidaspow drag model gives a better prediction of the time-averaged solid volume fraction distribution and axial velocity describing a core annular flow, and is therefore chosen for the heat transfer evaluation.

In regards to the heat transfer, the conservation of energy equation was solved. It was looked at how it can be coupled to the hydrodynamics. Thermal properties applicable for multiphase flows were investigated, and coupled to the hydrodynamics by making them dependent on the volume fraction of each phase. These include the effective thermal conductivity obtained by Zehner and Schlünder [54], and the absorption and scattering coefficient for particulate media as defined in Modest [9]. The DO-Radiation model was chosen to describe the radiation occurring within the IH-BFBSR, due to its broad applicability.

The mixture temperature, total surface heat flux and wall-to-bed heat transfer coefficient were evaluated. For the case without radiation, a strong temperature gradient could be observed near the wall. The bed does not heat up as fast with only a mean temperature difference of about 9 ^{o}C between 1-10 seconds at a height of 0.8 m. A strong positive linear relationship could be observed between the surface heat flux, effective thermal conductivity, wall-to-bed heat transfer coefficient and the solid volume fraction, and a negative linear relationship between the temperature and the solid volume fraction.

For the case with radiation included, a big temperature difference of 300 ^{o}C can be observed between 1-7 seconds at a height of 0.8 m. The bed heats up really fast due to the DO-Radiation model over predicting the amount of radiation that's emitted and scattered from the mixture. No strong temperature gradient can be observed near the wall. Again a strong positive linear relationship could be observed between the surface heat flux, absorption coefficient, wall-to-bed heat transfer coefficient and the

solid volume fraction, and a negative linear relation ship between the temperature and the solid volume fraction. There's still insufficient data on the coupling of radiative heat transfer in multiphase flows to its hydrodynamics where both phases are present in significant fractions and it needs further investigation.

6.2. RECOMMENDATIONS

As for future work, experimental validation is highly recommended to determine the accuracy of the results produced in this thesis. A number of assumptions were made for the the multiphase modelling such as the particles being spherical and uniform in size. Comparing with experimental results will give more insight into how the current model and assumptions can be improved and what parameters should be investigated next.

Properties of interest for the evaluation of the models by comparing the numerical results to experimental results include:

- Bubble shape and growth in size.
- Velocity measured at different sections in the IH-BFBSR.
- Pressure measured at different sections in the IH-BFBSR.
- Temperature measured at different sections in the IH-BFBSR.

In regards to the hydrodynamics in the IH-BFBSR, the CFD models can generally be improved by:

- Mesh Independency Test: decreasing the mesh size in order to improve numerical accuracy and evaluate whether the hydrodynamic results are mesh-independent.
- A 3D simulation.
- Implementing higher order discretization schemes to reduce the numerical errors.
- Implementing multiple particle sizes.
- Implementing temperature dependent properties such as the density and viscosity.
- Further parameter investigation, such as the restitution coefficient and wall functions.

In regards to the heat transfer in the IH-BFBSR, the CFD models can generally be improved by:

- Implementing temperature dependent properties such as the specific heat.
- Research into the optical properties of corundum particles at high temperatures, and implementing these values in the radiation model.
- Further parameter investigation, evaluating the absorption coefficient, scattering coefficient, and linear anisotropic function at different values than used under current assumptions.
- Evaluating other modified RTE's, such as the P-1 model in ANSYS® FLUENT.
- Defining a custom modified RTE, based on emperical analysis.
- Performing the CFD simulation in an open source software like OpenFOAM®, which gives the user more freedom to alter and/or define models, compared to a commercial software like ANSYS FLUENT®.

Assuming the heat transfer will be solved, the input and gasification of biomass particles, but also the combustion process taking place within the radiant tubes, could be included in the modelling of the IHBFB-SR.

BIBLIOGRAPHY

[1] *BP Statistical Review of World Energy*, techreport (BP, 2019) https://www.bp.com/content/dam/bp/business-sites/en/global/corporate/pdfs/energy-economics/statistical-review/bp-stats-review-2019-full-report.pdf .

[2] Eurima, *Trias energetica: the smart approach to climate neutrality,* http://www.eurima.org/energy-efficiency-in-buildings/trias-energetica.html .

[3] P. Basu, *Biomass gasification, pyrolysis and torrefaction : practical design and theory*, 2nd ed. (Academic Press., 2013).

[4] M. Bandyk, *Duke's Edwardsport IGCC still dealing with technical problems*, Tech. Rep. (IEEFA, 2013).

[5] M. Lackner, *Combustion science and technology,* in *KirkOthmer Encyclopedia of Chemical Technology* (American Cancer Society, 2011) pp. 1–40.

[6] P. Nag, *Power Plant Engineering*, 3rd ed. (New Delhi: McGraw Hill Education (India), 2015).

[7] P. Basu, *Combustion and gasification in fluidized beds,* (CRC/Taylor & Francis, 2006) Chap. 3, p. 59.

[8] J. Lundberg, *CFD study of a bubbling fluidized bed*, Master's thesis, Telemark University College (2008).

[9] M. Modest, *Radiative Heat Transfer* (Elsevier Science, 2013).

[10] C. L. Tien and B. L. Drolen, *Thermal radiation in particulate media with dependent and independent scattering,* in *Annual review of numerical fluid mechanics and heat transfer. Volume 1 (A88-18971 06-34). Washington, DC, Hemisphere Publishing Corp., 1987, p. 1-32.*, Vol. 1 (1987) pp. 1–32.

[11] *ANSYS Fluent Theory Guide.* (ANSYS, Inc., 2013).

[12] D. Geldart and A. Abrahamsen, *Homogeneous fluidization of fine powders using various gases and pressures,* Powder Technology **19**, 133 (1978).

[13] J. R. Grace, *Contacting modes and behaviour classification of gas-solid and other two-phase suspensions,* The Canadian Journal of Chemical Engineering **64**, 353.

[14] V. M. Schouten, *Design and Process Modeling of a New Indirectly Heated Fluidized Bed Steam Reformer*, Master's thesis, Technical University Delft (2015).

[15] A. Gomez-Barea and B. Leckner, *Modeling of biomass gasification in fluidized bed,* Progress in Energy and Combustion Science - PROG ENERG COMBUST SCI **36**, 444 (2010).

[16] H. Korbee, B. Smolders, and F. Stofberg, *Milieu voorop bij uitwerking van een globaal bestemmingsplan,* BOUW **22** (1979).

[17] O. L. D. Kunii and H. Brenner, *Fluidization Engineering*, 2nd ed. (Wiley, 1969).

[18] C. van der Meijden , *Development of the MILENA gasification technology for the production of Bio-SNG*, Ph.D. thesis, Department of Chemical Engineering and Chemistry (2010).

[19] J. Karl, *Biomass heat pipe reformer design and performance of an indirectly heated steam gasifier,* Biomass Conversion and Biorefinery **4**, 1 (2014).

[20] S. Karellas, J. Karl, and E. Kakaras, *An innovative biomass gasification process and its coupling with microturbine and fuel cell systems,* Energy , 284 (2008).

[21] F. Zuiderweg and A. Drikenburg, *Design report on fluidization,* , 133 (1967).

[22] S. Ergun and A. Orning, *Fluid flow through packed columns,* Journal of Chemical Engineering Progress **48** (1952).

[23] P. B. Whalley, *Handbook of multiphase systems,* Journal of Fluid Mechanics **129** (1982).

[24] H. Baehr, *Thermodynamik*, 14th ed. (Springer, 2009) pp. 68 – 69.

[25] H. Baehr and K. Stephan, *Heat and Mass Transfer*, 3rd ed. (Springer, 2011).

[26] J. Kuipers, W. Prins, and W. van Swaaij, *Numerical calculation of wall-to-bed heat transfer coefficients in gas-fluidized beds,* AIChE journal **38**, 1079 (1992).

[27] H. Hofgren, *Modelling and Experimental Investigations on Thermal Radiation in Combustion Environments*, Master's thesis, Lund University (2015).

[28] G. Mie, *Beiträge zur Optik trüber Medien, speziell kolloidaler Metallösungen* (1908).

[29] R. V. Dunkle, *Emissivity and Inter-Reflection Relationships for Infinite Parallel Specular Surfaces,* in *Thermal Radiation of Solids*, edited by S. Katzoff (1965) p. 39.

[30] J. F. Davidson and D. Harrison, *Fluidised particles,* AIChE Journal **10** (1963).

[31] M. Rhodes and D. Geldart, *A model for the circulating fluidized bed,* Powder Technology **53**, 155 (1987).

[32] J. Ding and D. Gidaspow, *A bubbling fluidization model using kinetic theory of granular flow,* AIChE **36**, 523 (1990).

[33] R. Lyczkowsky, I. Gamwo, F. Dobran, H. Ali, B. Chao, M. Chao, M. Chen, and D. Gidaspow, *Validation of computed solids hydrodynamics and pressure oscillation in bubbling atmospheric fluidized bed.* Powder Technology , 65 (1993).

[34] K. Anderson, S. Sundaresan, and R. Jackson, *Instabilities and the formation of bubbles in fluidized beds.* Journal of Fluid Mechanics **303**, 327 (1995).

[35] S. Benyahia, H. Arastoopour, T. Knowlton, and H. Massah, *Simulation of particles and gas flow behavior in the riser section of a circulating fluidized bed using the kinetic theory approach for the particulate phase.* Powder Technology **112**, 24 (2000).

[36] B. Sun and D. Gidaspow, *Computation of circulating fluidized bed riser flow for the fluidization.* Industrial Engineering Chemistry Research **38**, 787 (1999).

[37] S. Champan and T. Cowling, *The Mathematical Theory of Non-Uniform Gases* (Cambridge University Press, 1961).

[38] C. Lun, S.B.Savage, D. Jeffrey, and N. Chepurnity, *Kinetic theories for granular flow: inelastic particles in couette flow and slightly inelastic particles in a general flow field,* Journal of Fluid Mechanics **140**, 223 (1984).

[39] J. Sinclair and R. Jackson, *Gas–particle flow in a vertical pipe with particle– particle interactions.* AIChE **35**, 1473–1486 (1989).

[40] D. Gidaspow, *Multiphase Flow and Fluidization: Continuum and Kinetic Theory Descriptions.* (Academic Press, 1994).

[41] J. Nieuwland, M. A. van Sint, A. A.M. Kuipers, and P. van Swaaij, *Hydrodynamic modeling of gas–particle flows in riser reactors.* AIChE **42**, 1569–1582. (1996).

[42] G. Balzer, O. Simonin, A. Boelle, and J.Lavieville, *A unifying modeling approach for the numerical prediction of dilute and dense gas–solid flow.* Proceedings of the Circulating Fluidized Bed V (1996).

[43] A. Neri and D. Gidaspow, *Riser hydrodynamics: simulation using kinetic theory.* AIChE **46**, 52–67 (2000).

[44] M. Chiesa, V. Mathiesen, J. Melheim, and B. Halvorsen, *Numerical simulation of particulate flow by the eulerian–lagrangian and the eulerian– eulerian approach with application to a fluidized bed.* Computers Chemical Engineering **29**, 52–67 (2005).

[45] L. Gibilaro, *Fluidization Dynamics*, 1st ed. (Butterworth-Heinemann, 2001).

[46] K. Papadikis, A. Bridgwater, and S. Gu, *CFD modelling of the fast pyrolysis of biomass in fluidised bed reactors, part a: Eulerian computation of momentum transport in bubbling fluidised beds.* Chemical Engineering Science **63**, 4218–4227 (2008).

[47] D. Gidaspow, R. Bezburuah, and J. Ding, *Hydrodynamics of circulating fluidized beds: Kinetic theory approach,* (1991).

[48] M. Syamlal and T. O'Brien, *Computer simulation of bubbles in a fluidized bed,* AIChE Symposium Series **85**, 22 (1989).

[49] J. Valle, *Micromeritics: The Technology of Fine Particles* (Pitman Publishing Corporation, 1948).

[50] M. Syamlal, W. Rogers, and T. O'Brien, *Mfix documentation theory guide,* (1993).

[51] S. Ogawa, A. Umemura, and N. Oshima, *On the equation of fully fluidized granular materials,* Zeitschrift für angewandte Mathematik und Physik ZAMP **31**, 483 (1980).

[52] D. G. Schaeffer, *Instability in the evolution equations describing incompressible granular flow,* Journal of Differential Equations **66**, 19 (1987).

[53] D. Gunn, *Transfer of heat or mass to particles in fixed and fluidised beds,* International Journal of Heat and Mass Transfer **21**, 467 (1978).

[54] P. Zehner and E. U. Schlünder, *Wärmeleitfähigkeit von schüttungen bei mäßigen temperaturen,* Chemie Ingenieur Technik **42**, 933 (1970).

[55] S. Biyikli, K. Tuzla, and J. C. Chen, *A phenomenological model for heat transfer in freeboard of fluidized beds,* The Canadian Journal of Chemical Engineering **67**, 230 (1989).

[56] M. da Graca Carvalho, T. Farias, and P. Fontes, *Predicting radiative heat transfer in absorbing, emitting, and scattering media using the discrete transfer method,* American Society of Mechanical Engineers, Heat Transfer Division, (Publication) HTD **160**, 17 (1991).

[57] P. Cheng, *Two-dimensional radiating gas flow by a moment method,* AIAA Journal **2** (1964).

[58] R. Siegel, *Thermal Radiation Heat Transfer, Fourth Edition* (Taylor & Francis, 2001).

[59] E. Chui and G. D. Raithby, *Computation of radiant heat transfer on a non-orthogonal mesh using the finite-volume method,* Numerical Heat Transfer Part B - Fundamentals **23** (1993).

[60] F. Taghipour, N. Ellis, and C. Wong, *Experimental and computational study of gas-solid fluidized bed,* Chemical Engineering Science - CHEM ENG SCI **60** (2005).

[61] L. Chanchal, *Studies on fluidized bed gasification of biomass,* Master's thesis, Jadavpur University (2013).

[62] D. Perrone and M. Amelio, *A preliminary study of hydrodynamics and heat transfer in a bubbling fluidized bed containing sand particle using cfd,* Energy Procedia **81**, 1041 (2015).

[63] G. Krishnamoorthy, R. Klosterman, and D. Shallbetter, *A radiative transfer modeling methodology in gas-liquid multiphase flow simulations,* Journal of Engineering **2014** (2014).

[64] M. Syamlal and T. O'Brien, *Fluid dynamic simulation of O_3 decomposition in a bubbling fluidised bed,* AIChE Journal **49**, 2793 (2003).

[65] S. Zimmermann and F. Taghipour, *Cfd modeling of the hydrodynamics and reaction kinetics of fcc fluidized-bed reactors,* Industrial Engineering Chemistry Research **44** (2005).

[66] J. Kischkat, S. Peters, B. Gruska, M. Semtsiv, M. Chashnikova, M. Klinkmüller, O. Fedosenko, S. Machulik, A. Aleksandrova, G. Monastyrskyi, Y. Flores, and W. T. Masselink, *Mid-infrared optical properties of thin films of aluminum oxide, titanium dioxide, silicon dioxide, aluminum nitride, and silicon nitride,* Appl. Opt. **51**, 6789 (2012).

[67] S. Muley and N. Ravindra, *Emissivity of electronic materials, coatings, and structures,* JOM: the journal of the Minerals, Metals Materials Society **66**, 616 (2014).

[68] A. Bridgwater, G. Evans, E. T. S. U. G. Britain), G. B. D. of Trade, and Industry, *An assessment of thermochemical conversion systems for processing biomass and refuse* (Harwell Laboratory, Energy Technology Support Unit, 1993).

A

UDF CODES FOR MATERIAL PROPERTIES

Appendix A includes the user defined functions specified for the effective thermal conductivity, absorption and scattering coefficient of the solid and gas phase. The user defined functions were written in Microsoft Visual Studio 2010, compatible with ANSYS Fluent version 16.1. Every UDF must contain the udf.h file inclusion directive (include "udf.h") at the beginning of the source code file, which enables both the definition of DEFINE macros and other ANSYS Fluent-provided macros and functions, and their inclusion in the compilation process.

In short, UDFs:

- Are written in the C programming language.
- Must be defined using DEFINE macros supplied by ANSYS Fluent.
- Must have an include statement for the udf.h file.
- Use predefined macros and functions to access ANSYS Fluent solver data and to perform other tasks.
- Are executed as interpreted or compiled functions.
- Are hooked to an ANSYS Fluent solver using a graphical user interface dialog boxes.

The UDF's are compatible both for serial and parallel processing.

A.1. EFFECTIVE THERMAL CONDUCTIVITY FOR SOLIDS AND GAS

```
#include "udf.h"
#include "math.h"

#define OMEGA 7.26E-3

/*Define Effective Thermal Conductivity solid*/
DEFINE_PROPERTY(conduct_solid,cell,thread)
{
#if !RP_HOST
  real k_sol;
  real T_s;
  real T_f;
  real K_S0;
  real K_F0;
  real a;
  real b;
  real c1;
  real t1;
  real t2;
  real gm;
  real c;
  real k_bs;
  real A1 = 85.868;
  real A2 = -0.22972;
  real A3 = 2.607E-4;
  real A4 = -1.3607E-7;
  real A5 = 2.7092E-11;
  real D1 = -0.008018;
  real D2 = 1.315;
  real D3 = 1.192E-5;
  real epsi_max = 1.-10*SD_EPS;
  real e_gas = MIN( epsi_max, (1.-C_VOF(cell,thread)));

  Thread *mix, *sol, *gas;
  mix = THREAD_SUPER_THREAD(thread);
  sol = THREAD_SUB_THREAD(mix,1);
  gas = THREAD_SUB_THREAD(mix,0);

c1 = C_VOF(cell,thread);
T_s = C_T(cell,sol);
T_f = C_T(cell,gas);

/*Temperature dependence microscopic Conductivity*/
K_S0 = A1+A2*T_s+A3*pow(T_s,2)+A4*pow(T_s,3)+A5*pow(T_s,4);
K_F0 = D1 + pow(T_f,D2)*D3; a = K_S0/K_F0;

b = 1.25*pow((1.-e_gas)/e_gas, 10./9.);
t1 = (a-1.)/pow((1.-b/a),2.0)*(b/a)*log(a/b);
t2 = -((b-1.)/(1.-b/a))-0.5*(b+1.);
gm = (2./(1.-b/a))*(t1+t2);
k_bs = K_F0*(OMEGA*a + (1.-OMEGA)*gm);
k_sol  = k_bs/sqrt(1.-e_gas);
return (k_sol);
#endif
}
```

```
/*Define Effective Thermal Conductivity gas*/
DEFINE_PROPERTY(conduct_gas,cell,thread)
{
    #if !RP_HOST
    real k_bf;
    real k_gas;
    real D1;
    real D2;
    real D3;
    real T_f;
    real K_F0;
    real c;
    D1 = -0.008018;
    D2 = 1.315;
    D3 = 1.192E-5;

c= C_VOF(cell,thread);
T_f = C_T(cell,thread);

/*Temperature dependence microscopic Conductivity*/
K_F0 = D1 + pow(T_f,D2)*D3; k_bf = K_F0*(1.-sqrt(1.-C_VOF(cell,thread)));
k_gas = k_bf/C_VOF(cell, thread);

 return (k_gas);
#endif
}
```

A.2. ABSORPTION AND SCATTERING COEFFICIENT

```
#include "udf.h"
#include "math.h"

/*Define absorption coefficient solids*/
DEFINE_PROPERTY(abs_solid,cell,thread)
{
#if !RP_HOST
  real abs_sol;
  real E = 0.9006;
  real d = 352E-6;
  real v_f;
  real N_T;
  v_f= C_VOF(cell,thread);  /*Call Volume fraction info from cell*/
  abs_sol = 3*v_f/(2*d)*E;
  return (abs_sol);
#endif
}

/*Define scattering coefficient solids*/
DEFINE_PROPERTY(scat_sol,cell,thread)
{
#if !RP_HOST
  real abs_sol;
  real E = 0.9006;
  real d = 352E-6;
  real v_f;
  real N_T;
  v_f= C_VOF(cell,thread);
  abs_sol = 3*v_f/(2*d)*(1-E);
  return (scat_sol);
#endif
}

/*Define absorption coefficient*/
 DEFINE_PROPERTY(abs_fluid,cell,thread)
{
#if !RP_HOST

  real C0 = -0.23093;
  real C1 = -1.12390;
  real C2 = 9.41530;
  real C3 = -2.99880;
  real C4 = 0.51382;
  real C5 = -1.8684e-05;
  real T_s;
  real T;
  real v_f;
  real abs_fluid;
  v_f= C_VOF(cell,thread); /*Call Volume fraction info from cell*/
  T_s = C_T(cell,thread);  /*Call Temperature info from cell*/
  T= 1000/T_s;

abs_fluid = (C0+C1*T +C2*pow(T,2)+C3*pow(T,3)+C4*pow(T,4)+C5*pow(T,5));
return (abs_fluid);
#endif
}
```

B

SINGLE PHASE MODELLING

Before implementing the multiphase flow, first a single phase flow simulation was performed in order to establish the broad flow pattern of the steam within the reactor. The values in Table 4.4 were used for the steam properties, and the inlet velocity was set to 0.2 m/s. Figure B.1 showcases the velocity contour plot at different time steps within the IH-BFBSR.

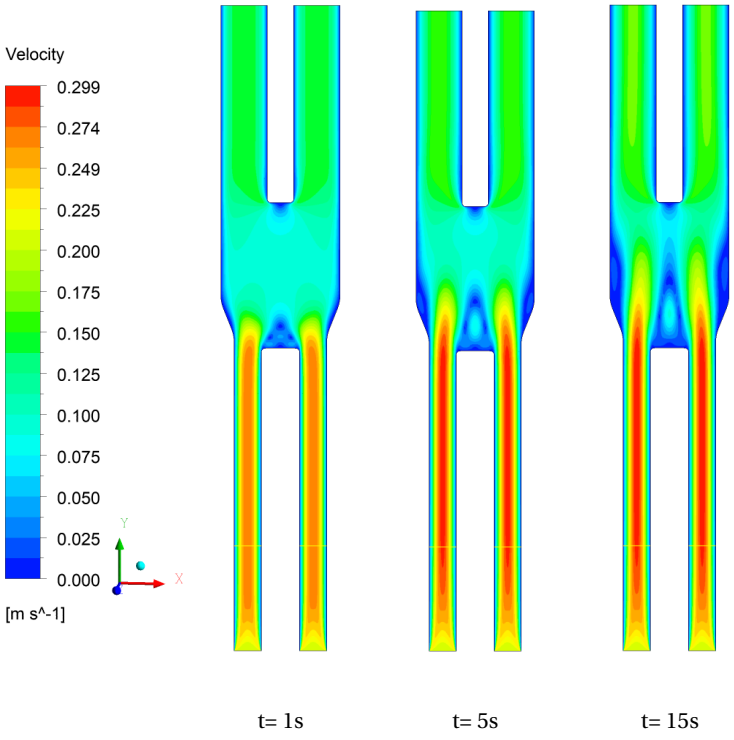

Figure B.1: Velocity profile of steam at different time steps.

The flow seems more or less symmetric within the reactor. The Reynolds number is equal to 112, which means the flow is considered laminar within the pipe. Figure B.2a showcases the velocity profile at different heights of the reactor and Figure B.2b the velocity along the length of the reactor measured at t= 20 s.

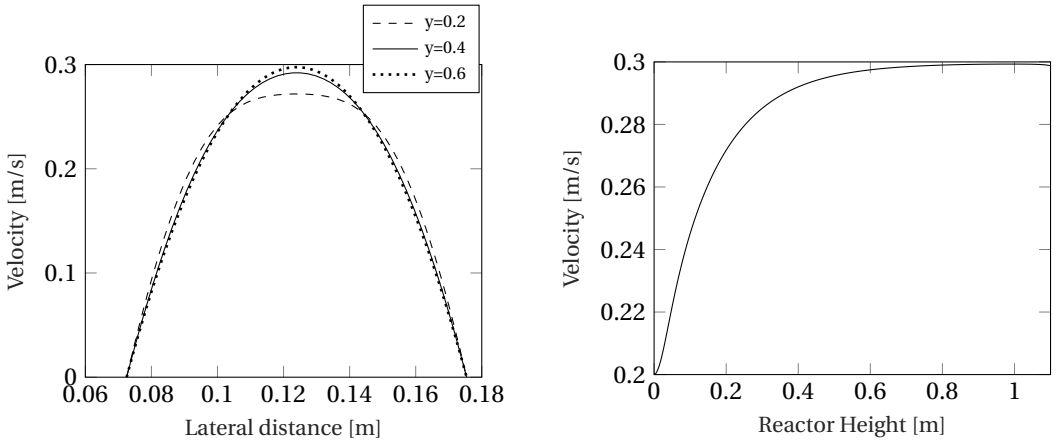

(a) Velocity profile in the lateral direction, measured at different heights at t= 20 s.

(b) Velocity profile along the central axis of inlet 2 at t= 20 s.

Figure B.2: Velocity profile for steam within the reactor.

As can be seen in Figure B.2b, the flow becomes fully developed around 0.8 m.

C

PARTICLE SIZE DISTRIBUTION

Ir. M. del Grosso performed a particle-size distribution analysis for the corundum particles using the MicroTrac S3500. Three different grain sizes were considered: F046; F054; F060. The results are shown in Figure C.1.

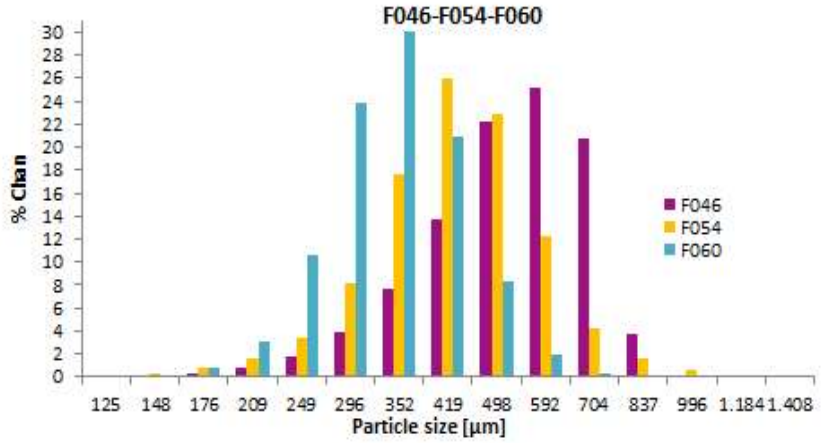

Figure C.1: Particle size distribution of corundum particles.

The main size obtained is 592 μm for F046, 419 μm for F054 and 352 μm for F060.

D

GASIFICATION REACTIONS

The chemistry of biomass gasification is complex. Biomass gasification proceeds primarily via a two-step process: pyrolysis followed by gasification. Pyrolysis is decomposition of the biomass feedstock by heat. This step, also known as devolatilization, is endothermic and produces 75 to 90% volatile materials in the form of gaseous and liquid hydrocarbons. The remaining nonvolatile material, containing a high carbon content, is referred to as char [68]. The volatile hydrocarbons and char are subsequently converted to syngas in the second step gasification. The reactions are summarized in Table D.1

Table D.1: Gasification reactions [14] [15].

EQ#	Name	Stoichiometry	Heat of reaction kJ/mol
Step 1	Drying		
1	-	$Biomass \longrightarrow Dry\,Biomass + H_2O$	>0
Step 2	Pyrolysis		
2	Devolatilization	$Dry\,Biomass \longrightarrow C + N + O + H + S + Ash$	>0
Step 3	(Partial) Oxidation		
3	Partial oxidation	$C(s) + 0.5\,O_2 \longrightarrow CO$	-111
4	CO oxidation	$CO + 0.5\,O_2 \longrightarrow CO_2$	-283
5	H_2 oxidation	$H_2 + 0.5\,O_2 \longrightarrow CO_2$	-242
6	CH_4 oxidation	$CH_4 + 0.5\,O_2 \longrightarrow CO + 2\,H_2$	-37.5
Step 4	Gasification and reforming		
7	Dry reforming	$CH_4 + CO_2 \longrightarrow 2\,CO + 2\,H_2$	-170
8	Wet reforming	$CH_4 + H_2O \longleftrightarrow CO + 3\,H_2$	206
9	Water-gas-shift	$CO + H_2O \longleftrightarrow CO_2 + H_2$	-41
10	Steam gasification	$C(s) + H_2O \longrightarrow CO + H_2$	131
11	Boudouard reaction	$C(s) + CO_2 \longrightarrow 2\,CO$	173
12	Hydrogen gasification	$C(s) + 2\,H_2 \longrightarrow CH_4$	-75
step 5	Tar conversion		
13	C_2H_4	$C_2H_4 + O_2 \longrightarrow 2\,CO + 2\,H_2$	>0
14	C_6H_6	$C_6H_6 + 3\,O_2 \longrightarrow 6\,CO + 3\,H_2$	>0
step 6	Tar reactions		
15	Tar oxidation	$CnHm + (n/2)\,O_2 \longrightarrow nCO + (m/2)\,H_2$	-
16	Dry reforming	$CnHm + nCO_2 \longrightarrow (m/2)\,H_2 + (2\,n)\,CO_2$	-
17	Tar steam reforming	$CnHm + nH_2O \longrightarrow (m/2 + n)\,H_2 + nCO_2$	-
18	Hydrogenation	$CnHm + (2\,n - m/2)\,H_2 \longrightarrow n\,CH_4$	-
19	Thermal cracking	$CnHm \longrightarrow (m/4)\,CH_4\,(n\text{-}m/4)\,C$	-